JOURNAL OF GEOPHYSICAL RESEARCH, VOL. 113, E05S90, doi:10.1029/2006JE002819, 2008

Click Here for Full Article

Search for magnetic minerals in Martian rocks: Overview of the Rock Abrasion Tool (RAT) magnet investigation on Spirit and Opportunity

Walter Goetz,[1,2] Kristoffer Leer,[2] Haraldur P. Gunnlaugsson,[3] Paul Bartlett,[4] Brandon Basso,[4] Jim Bell,[5] Preben Bertelsen,[2] Charlotte S. Binau,[2] Phillip C. Chu,[4] S. Gorevan,[4] Mikkel F. Hansen,[6] Stubbe F. Hviid,[1] Kjartan M. Kinch,[5] Göstar Klingelhöfer,[7] Alastair Kusack,[4] Morten B. Madsen,[2] Douglas W. Ming,[8] Richard V. Morris,[8] Erik Mumm,[4] Tom Myrick,[4] Malte Olsen,[2] Steven W. Squyres,[5] Jack Wilson,[4] and Albert Yen[9]

Received 23 August 2006; revised 3 June 2007; accepted 11 October 2007; published 21 May 2008.

[1] The Rock Abrasion Tool (RAT) on board the Mars Exploration Rovers (MER) is a grinding tool designed to remove dust coatings and/or weathering rinds from rocks and expose fresh rock material. Four magnets of different strengths that are built into the structure of the RAT have been attracting substantial amounts of magnetic material during RAT activities from rocks throughout both rover missions. The RAT magnet experiment as performed on Spirit demonstrates the presence of a strongly ferrimagnetic phase in Gusev crater rocks, which based on Mössbauer and visible/near-infrared reflectance spectra is interpreted as magnetite. The amount of abraded rock material adhering to the magnets varied strongly during the mission and is correlated in a consistent way to the amount of magnetite inferred from Mössbauer spectra for the corresponding rock. The RAT magnet experiment as performed on Opportunity also indicates the presence of a strongly ferrimagnetic phase in outcrops, such as magnetite or an altered version of magnetite. However, the evidence is weaker than in the case of Spirit. According to data from the α particle X-ray spectrometer (APXS) and the Mössbauer spectrometer (MB), the Eagle crater outcrops should not contain magnetite and their magnetization should not exceed 0.03 A m^2 kg^{-1}. However, this assertion seems to be in contradiction with the results of the RAT magnet experiment. The evidence for a strongly ferrimagnetic phase at low abundance in the Meridiani outcrops is discussed.

Citation: Goetz, W., et al. (2008), Search for magnetic minerals in Martian rocks: Overview of the Rock Abrasion Tool (RAT) magnet investigation on Spirit and Opportunity, *J. Geophys. Res.*, *113*, E05S90, doi:10.1029/2006JE002819.

1. Introduction

[2] The 2003 Mars Exploration Rovers (MERs) (http://athena.cornell.edu [*Squyres et al.*, 2003]) are equipped with an instrument positioning system (IPS) that consists of an instrument deployment device (IDD) and associated sensors and software to model and control the IDD. The IDD carries four payload elements: The Microscopic Imager (MI), the Mössbauer spectrometer (MB), the α particle X-ray Spectrometer (APXS) and the Rock Abrasion Tool (RAT). The RAT [*Gorevan et al.*, 2003] is configured with a spinning grinding tool and a spinning brush, both mounted on a rotating planetary gear. Four permanent magnets of different strengths mounted in the lower part of the RAT housing near the grinding head and the brush have been attracting particles produced by abrasion during a large number of grinding processes over more than 400 sols on both landing sites.

[3] The RAT magnet experiment was originally designed to complement Mössbauer spectroscopy, and to search for ferrimagnetic phases that might be present below the sensitivity of Mössbauer spectroscopy. Early in the devel-

[1]Max-Planck-Institut für Sonnensystemforschung, Katlenburg-Lindau, Germany.
[2]Niels Bohr Institute, University of Copenhagen, Copenhagen, Denmark.
[3]Institute of Physics and Astronomy, University of Aarhus, Aarhus, Denmark.
[4]Honeybee Robotics, New York, New York, USA.
[5]Department of Astronomy, Cornell University, Ithaca, New York, USA.
[6]Department of Micro- and Nanotechnology, Danish Technical University, Lyngby, Denmark.
[7]Institute for Inorganic and Analytical Chemistry, Johannes Gutenberg-Universität, Mainz, Germany.
[8]NASA Johnson Space Center, Houston, Texas, USA.
[9]Jet Propulsion Laboratory, California Institute of Technology, Pasadena, California, USA.

Copyright 2008 by the American Geophysical Union.
0148-0227/08/2006JE002819$09.00

opment phase of the mission, a skirt mounted around the RAT was conceived to protect the instruments on the rover against contamination by the particles that would be generated during brushing and grinding of rocks. Such a skirt would have promoted the capture of magnetic grains by the RAT magnets, but would have partially obstructed viewing of these magnets by the panoramic camera (Pancam) located on the rovers' masts. The RAT skirt concept, though later discarded, motivated the implementation of two sets, rather than one set of RAT magnets into the RAT housing.

[4] The basic characteristics of the RAT magnets have been described previously [*Madsen et al.*, 2003; *Gorevan et al.*, 2003]. The term "RAT magnet" refers to the entire device composed of permanent magnet (Sm_2Co_{17}) and aluminum housing. A cylindrical magnet is positioned at a well-defined depth below the diffusely reflecting aluminum surface that is exposed to the Martian environment. This surface is referred to as the active surface of the RAT magnet and can be seen as a circular region (5.92 mm in diameter) in most images. The relative locations of the RAT magnets (RM) are shown in Figure 1a: Two strong, identical RAT magnets, referred to as "RM 1_2" and "RM 1_3," are located at opposite sides on the bottom of the RAT. In addition, a weak magnet (RM 2) and a very weak magnet (RM 3) are mounted next to RM 1_2 and RM 1_3, respectively. Parameters characterizing location and magnetic strength of each RAT magnet are summarized in Table 1. The resulting magnetic fields and field gradients are plotted in Figures 1b–1d.

[5] During RAT operations the active surface of each RAT magnet is located 4 to 5 mm above the rock surface. Assuming an abraded rock particle to be magnetized along the local magnetic field, the attractive magnetic force applied to that particle is proportional to the product of its magnetization σ [A m^2 kg^{-1}] and the field gradient ∇B [T m^{-1}]. The magnetic field will create that magnetization, if the ferrimagnetic particle that approaches the magnets has not been magnetized before [*Madsen et al.*, 2003].

[6] According to the coordinate system sketched in Figure 1a the active surfaces of the magnets are contained in the (x, y) plane at z = 0, which is also the plane of the revolve housing cap. The *z* axis is perpendicular to that plane. The *x* axis contains the centers of the active surfaces of RAT magnets 1_2 and 2 (or 1_3 and 3). Now refer to Figure 1b. The center of RAT magnet 1 has been arbitrarily positioned at x = 10 mm. The centers of RAT magnets 2 and 3 are then positioned at x = 18.09 mm. The top (red) and bottom (blue) curves refer to the components of magnetic field and magnetic field gradient, respectively. The projections of field vector and field gradient vector along x, y, and z direction are represented by solid, dashed and dotted lines, respectively. RAT magnet 3 has a smaller field and field gradient vector along any direction as compared to RAT magnet 2. Therefore the curves referring to RAT magnets 2 and 3 can be easily distinguished from each other, although they are displayed by the same line type. Note that the projections along the y direction are all zero due to symmetry with respect to the (x, z) plane. Neighbor magnets are mounted with antiparallel orientation. Therefore the B_z components of strong (RM 1) and weak magnets (RM 2 or 3) have opposite sign.

[7] Figures 1c and 1d display the absolute values of magnetic fields and field gradients, respectively, at different (constant) heights above the active surface (z = 0, 1, 2, 3, 4 and 5 mm). Both quantities have a local minimum in the region between strong and weak magnet (x $\sim$ 14 to 16 mm). This minimum is shallow at several millimeters above the active surface, but becomes very pronounced within a millimeter from that surface as a result of the antiparallel mounting of the samarium-cobalt magnets. Abraded rock particles are subjected to any magnetic field and field gradient that range from zero and up to some maximum value (as specified in Table 1). For later reference we note that particles located within 1–2 mm thick accumulations on the strong magnet (as frequently observed on Mars as well as during simulation experiments on Earth) experience fields and field gradients equal to at least 0.05 T and 50 T m^{-1}, respectively.

[8] The RAT magnets have been accumulating magnetic grains from many different kinds of rocks (especially on Spirit), as well as airborne dust (either fallen out from the atmosphere or lifted up from rock surfaces by the action of the brush). As long as all the abraded rocks belong to the same compositional class (A sol < 150 and B sol < 65), we can still analyze the data, as if they were all part of a long-lasting "one-shot experiment." Later on, different types of particles have been accumulating on the RAT magnets on top of each other. Some particles may have also been removed from the magnets by episodes of strong wind or by the impact of new, strongly magnetic particles.

[9] The present paper consists of three major sections. Section 2 describes the "monorock experiment" early during the mission, as it has been performed on rocks/outcrops of similar chemistry and mineralogy: unaltered olivine basalts (Adirondack, Humphrey) in Gusev crater and hematite- and sulfate-rich outcrops at Meridiani Planum. The amount of material clinging to the strong RAT magnets will be determined and the implications for the nature of the magnetic phase as accumulated or enriched on the magnets will be discussed. Section 3 will describe the "multirock experiment" as it evolved at both landing sites over several hundred sols. It will be shown, how the RAT magnets did react to grinding into a variety of rocks with strongly differing magnetic properties. Finally, section 4 will describe some RAT magnet simulations performed in the laboratory. The new insight gained from these simulation experiments will be used to comment and refine conclusions that have been drawn in sections 2–4.

[10] A few words on notation and terminology in the present paper: RAT magnet observations are referred to by the sol number when the RAT magnets were imaged, not when the corresponding grind has been performed. The RAT magnet experiment relies exclusively on Pancam images that are either calibrated to absolute radiometric units (W m^{-2} sr^{-1} nm^{-1}) or to radiance factors (I/F). Accordingly, they are labeled as "RAD" or "IOF" calibrated images, respectively [*Bell et al.*, 2006]. Spectra shown in the present paper are based on I/F data and shall only be interpreted as relative spectra. It is reasonable to scale these spectra by some constant (wavelength-independent) factor, provided that the brightness of the target surface is chiefly controlled by direct, incident sunlight

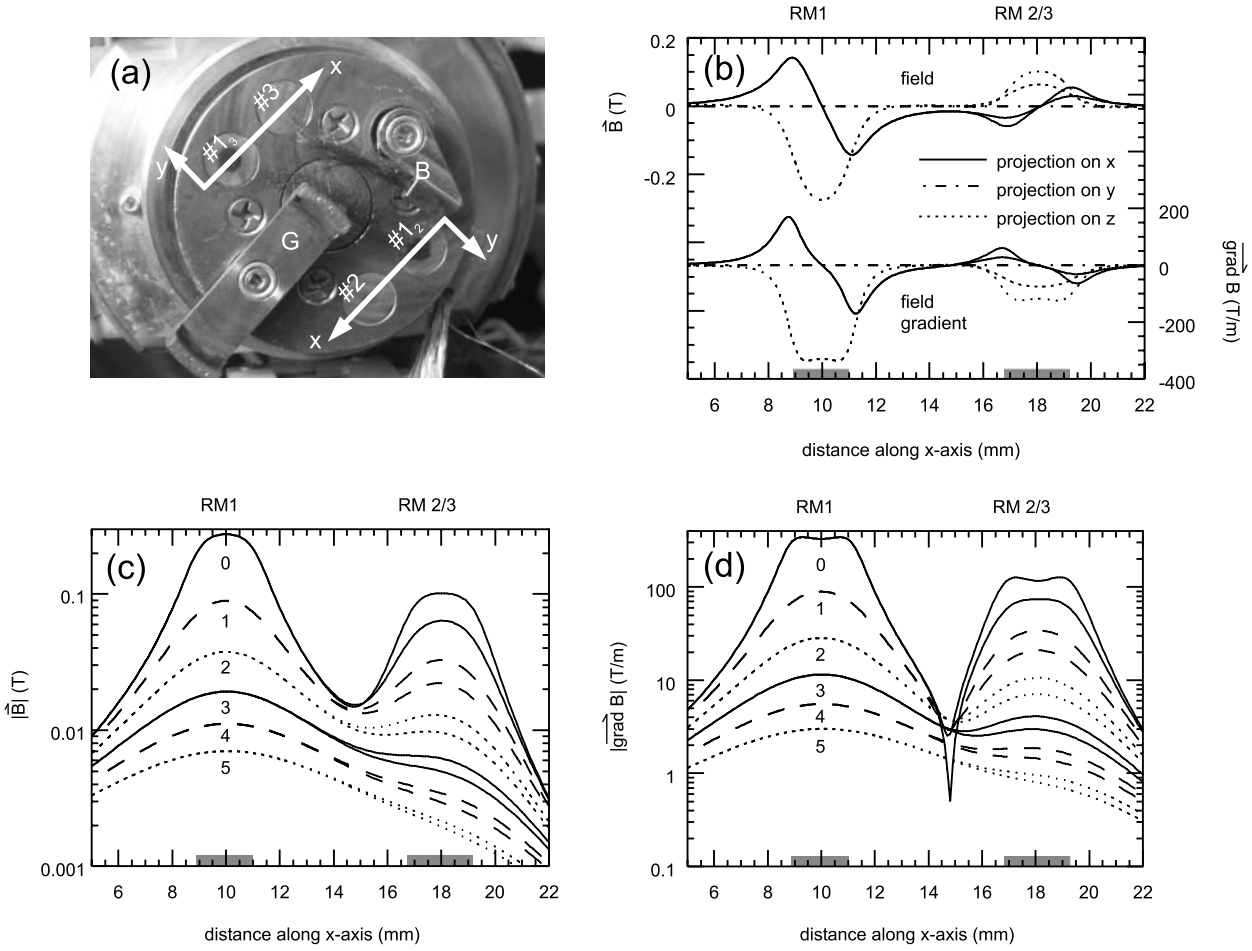

Figure 1. Mounting (Figure 1a) and magnetic strength (Figure 1b) of the RAT magnets. (a) Image of the RAT-EM revolve housing (33.4 mm in diameter). The RAT magnets can be seen as four circular insets. Grinding head and rotate brush are marked by "G" and "B," respectively. A second brush, the so-called revolve brush, can be seen in the lower right part of the image. Starting from the grinding head in the clockwise direction: RAT magnet 1_3, 3, rotate brush, 1_2, 2 with $1_2 \sim 1_3 > 2 > 3$ in terms of magnetic strength. (b) Vector components of magnetic field $\vec{B}$ (left ordinate) and field gradient $\vec{\nabla}B$ (right ordinate) across the active surface (z = 0 mm) of the RAT magnets (RM) 1, 2 and 3. (c, d) Absolute value of $\vec{B}$ and $\vec{\nabla}B$ at different heights (z = 0, 1, 2, 3, 4, and 5 mm) above the magnet. z = 0 mm refers to the active surface. The magnets are centered at 10.00 and 18.09 mm. Their positions are indicated by the means of gray, semitransparent rectangles.

rather than sky light. The scaling of spectra is addressed in Appendix C.

[11] Pancam images shown in this paper are labeled by landing site (A, B), sol number and filter number (e.g., L2, L3; compare Appendix A). Image coordinates are specified by column and row number with the coordinates (0,0) denoting the first CCD pixel that is read out (in left eye Pancam images, this pixel is located in the upper left corner

Table 1. Size and Magnetic Strength of the RAT Magnets[a]

	RM 1 (Strong)	RM 2 (Weak)	RM 3 (Very Weak)
Diameter of Sm_2Co_{17} magnet, mm	2.25	2.50	2.50
Height of Sm_2Co_{17} magnet, mm	4.00	0.50	0.50
Distance from active surface to closest magnet surface, mm	0.60	0.80	1.20
$\lvert\nabla B_z\rvert$ [T m^{-1}] (maximum value)	350	120	80
$\lvert B\rvert$ [T] (maximum value)	0.27	0.10	0.06
Range of B_x [T]	[−0.14, 0.14]	[−0.06, 0.06]	[−0.03, 0.03]
Range of B_z [T]	[−0.27, 0]	[0, 0.10]	[0, 0.06]

[a]RM RAT magnets. All three types of magnets are built into the bottom plane of the RAT. The strong type (RM 1) is used twice. The magnetic fields and field gradients refer to the active surface. These values have been calculated and confirmed to within 10% as part of the outgoing inspection of the flight modules.

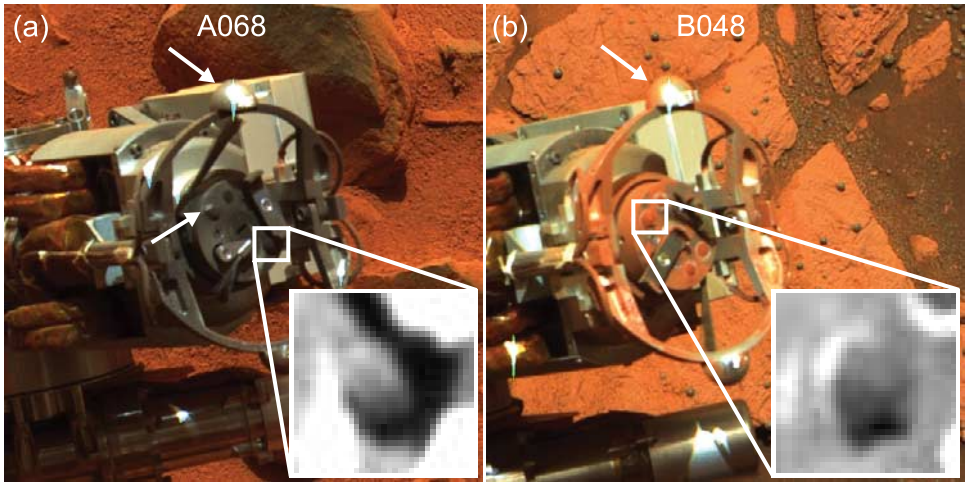

Figure 2. False color composite Pancam images (L2, L5, L7) of the RAT magnets. (a) A068. The inset shows the magnet particle accumulation as seen through the filter L6 (480 nm). (b) Same as Figure 2a but for B048. The color images have been generated in a controlled way (with the RGB components stretched from 0 to 0.05 W m^{-2} sr^{-1} nm^{-1}). The scene is brighter on B048 as compared to A068. Note the difference in color between A068 and B048 magnetic particles. Two arrows point to the upper RAT contact balls (A068, B048). A third arrow points to the A068 RAT magnet 1_2 that has received a significant amount of scattered light from the nearby contact ball.

of the image frame). All color images are false color composites of L2 (750 nm), L5 (535 nm), and L7 (440 nm) RAD calibrated images that are stretched from zero and up to some common radiometric level (in W m^{-2} sr^{-1} nm^{-1}). As a result, color and brightness of these images can be compared to each other on a relative level. The stretch parameters are specified in the Figure 2, 7, 10, and C1 captions.

2. Early Results of the RAT Magnet Experiment

2.1. Basic Findings

[12] Figure 2 shows color images of the RAT revolve housing cap from sols A068 and B048. We note immediately the particle accumulation on the strong RAT magnets on both rovers. The amount of material on these magnets must be significant, given the strong luminosity gradient across the magnets. We also note the profound difference in color between A068 (basically gray) and B048 (reddish) as quantified by the visible/near-infrared spectra shown in Figure 3. The dark, grey spectra of RAT magnet material from the rocks Adirondack (A035, not shown) and Humphrey (pre-RAT A057, post-RAT A068, Figure 3) can be ascribed to magnetite. The conclusion is based on the detection of significant amounts of magnetite in these rocks by Mössbauer spectroscopy [*Morris et al.*, 2004, 2006a]. However, the material on the RAT magnets is not composed of pure magnetite but rather consists of magnetite-rich basaltic grains.

[13] Opportunity RAT magnet particles are distinctly red. Their spectra are shown in Figure 3. For reference, we also show spectra of classical Martian bright regions that have been acquired by Earth-based telescopes [*Singer et al.*, 1979; *Bell et al.*, 1990; *Mustard and Bell*, 1994]. Since all spectra have been scaled to 5% at 440 nm, they can only be compared to each other in terms of relative (not absolute) reflectance. Depending on their average slope in the region 550–750 nm, two different spectral types may be identified: reflectance spectra with moderate slope (post-RAT McKittrick B031, post-RAT Flatrock/Mojo B045 and B048) and those with a stronger slope (post-RAT Guadalupe B035). In that sense Guadalupe seems to differ from McKittrick (that was abraded before Guadalupe) and Flatrock/Mojo (abraded after Guadalupe). Similar features have been seen in the reflectance spectra of RAT hole interior and associated RAT cuttings for these targets [*Farrand et al.*, 2007].

[14] The B048 magnetic particle accumulation has a somewhat different appearance as compared to A068 (compare monochromatic insets in Figure 2). There might be a difference in shape between both particle accumulations due

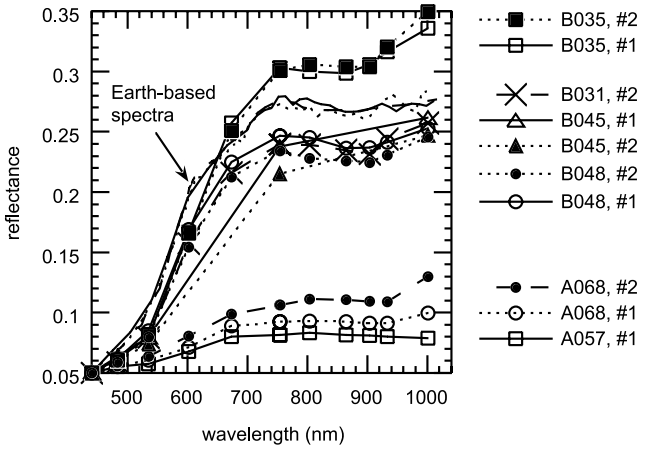

Figure 3. Visible/near-infrared spectra of RAT magnets 1_3 and 2. All spectra scaled to 5% at 440 nm. The grayish spectra have been acquired by MER-A, the red spectra by MER-B. The spectra of B035 have a particularly strong blue-to-red slope. Earth-based telescopic spectra of classical bright Martian regions [*Singer et al.*, 1979; *Bell et al.*, 1990; *Mustard and Bell*, 1994] are also shown for reference.

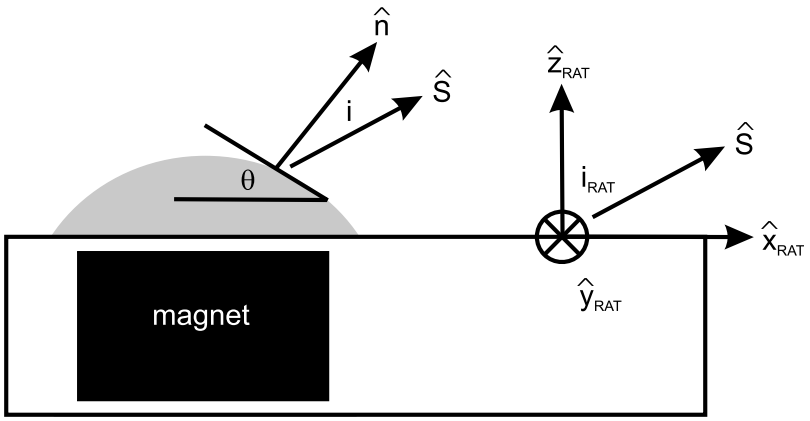

Figure 4. Parameters for radiometric modeling. The grey area represents magnetic particles that are accumulated nearby the RAT magnet on the revolve housing cap plane; $\hat{n}$ is the local normal vector of a small area of the particle accumulation, and $\hat{S}$ is the unit vector pointing to the Sun. The unit vectors ($\hat{x}_{RAT}$, $\hat{y}_{RAT}$, $\hat{z}_{RAT}$) define the RAT frame. These vectors define a series of angles (i, θ, i_{RAT}) that are needed for radiometric modeling (refer to the text). In addition, an azimuth angle (denoted ϕ, see text) is needed if the profile across the particle accumulation does not follow the direction of the incident solar light as projected onto the revolve housing cap plane.

differences in size distribution, cohesive properties and/or magnetic properties of captured particles. Different size distributions are certainly expected, given the strongly different mechanical properties (e.g., softness, porosity) of Gusev plains basalts and Eagle crater outcrops [*Squyres et al.*, 2004]. However, a more likely explanation is a somewhat inhomogeneous illumination of the B048 particle accumulation due to significant light scattering by the upper contact ball (see arrow in Figure 2b) of the RAT contact sensing and preload structure.

[15] During radiometric analysis of the B048 image (section 2) care has been taken to prevent this light scattering component to affect the results of this analysis. In the case of A068, light scattering from the contact ball has indeed strongly affected the brightness of RAT magnet 1_2 (see arrows in Figure 2a), which, however, has not been analyzed in the present paper.

[16] While the amount of material clinging to strong and weak RAT magnets did vary over the mission (both in an absolute and a relative sense), the material accumulated on both types of magnets has been found to be similar from a spectral point of view. The amount and the magnetic properties of particles accumulated on RAT magnet 1_3 will be assessed in greater detail below.

2.2. Quantitative Approach

2.2.1. The Model: Shape From Shading

[17] As noted in section 2.1, the A068 and B048 images show luminosity gradients across the material on the strong RAT magnets. Such gradients are most prominent in the blue region of the spectrum, where the incident radiance is more strongly dominated by direct solar light as compared to diffuse sky light. Moreover, when imaging small targets (such as the RAT magnets) through a short-wavelength (blue) filter, we benefit from the higher resolution (quantified by the MTF value [*Bell et al.*, 2003]) of the camera as compared to the red/NIR filters. In the following, Lambert's law will be applied to RAD calibrated images (A068, B048) acquired through Pancam's left eye filter L6 ($\lambda = 480$ nm) in order to infer the amount of material clinging to the magnets from the luminosity gradients. The focus will be on RAT magnet 1_3, rather than on 1_2, since the material on the latter one is most often disturbed by twisted bristles of the rotate brush. The method, generally referred to as photoclinometry or "shape from shading" has been often applied to remotely imaged planetary surfaces and in particular to crater morphometry [*Davis and Soderblom*, 1984; *Horn and Brooks*, 1989; *Craddock et al.*, 1997]. The problem considered here is much simpler, since the area analyzed is small (measuring 1 cm at target and 20 (pixels (px) in image frame) in image space) and assumed to be uniform in terms of chemistry and mineralogy. In addition this work uses particular constraints on the lighting-viewing geometry at each pixel as well as constraints on the topology of the RAT magnet material (e.g., its convex shape). Such constraints would not be available for general photoclinometry on remotely imaged surfaces. The output of this model is a one-dimensional topographic profile (in mm) across the material on the RAT magnets.

[18] The primary input to the radiometric analysis of these images is the lighting geometry of the revolve housing cap plane (hereinafter referred to as RHCP). The normal to this plane is called the RAT centerline and a vector originating in any point on the revolve housing cap and pointing in the grind direction (thus pointing away from the revolve housing) is referred to as RAT centerline vector (Figure 4). The angle between the RAT centerline vector and a vector pointing to the Sun is called the incident angle, denoted i_{RAT}. Full information on the lighting-viewing geometry would also include emission angle (denoted e_{RAT}) and phase angle (denoted g_{RAT}), although these angles do not play any significant role in the present paper. The simple radiometric analysis envisaged here requires the following four steps to be performed:

[19] 1. Select the data: A series of pixels (radiances) located along a straight line are selected for further analysis as described in section 2.2.2.

[20] 2. Determine the cosine of the local solar incidence angle: Lambert's law is used to infer the cosine of the incidence angle (noted i, referring to a particular local facet of the magnetic particle accumulation, Figure 4; see also notation section) pixel by pixel from the radiance profile (noted I):

$$I = A_L + \cos(i)B_L \tag{1a}$$

According to equation (1), the luminosity of a local facet of the magnetic particle accumulation is composed of reflected skylight (A_L) and reflected direct sunlight ($\cos(i)B_L$). We thus assume the radiance gradient across the magnetic particle accumulation to be controlled by the cosine of the local solar incidence angle. We also assume isotropic illumination by the Martian sky and neglect any potential dependence of the radiance on the local emission angle (e) and phase angle (g).

[21] Before being able to convert the radiance (I) pixel by pixel to cos(i) by the means of (1a), we need to determine the Lambert parameters (A_L, B_L). This is done by the means of the following boundary conditions:

$$I_{min} = A_L + \cos(i_{max})B_L \tag{1b}$$

$$I_c = A_L + \cos(i_{RAT})B_L \tag{1c}$$

where I_{min} and I_c denote the minimum radiance near the shadow region and the radiance in the center of the magnetic particle accumulation, respectively. The local facet at the latter location is assumed to be parallel to the RHCP. Therefore the local solar incidence angle (i) is equal to i_{RAT} at that location.

[22] We still need the value of i_{max} in order to find the Lambert parameters. If the magnetic particle accumulation casts a true shadow, then we can write

$$\cos(i_{max}) = 0 \Leftrightarrow i_{max} = 90^\circ \Leftrightarrow A_L = I_{min} \tag{2}$$

However, in both cases (A068, B048) I_{min} turns out to be somewhat larger than typical shadow radiances observed on the RHCP implying $i_{max} < 90^\circ$ (compare (1b)). The precise value of i_{max} has been determined by an iterative method (compare step 4).

[23] The local solar incidence angle (i) is related to the local facet tilt angle (θ, Figure 4) by

$$\cos(i) = \sin(i_{RAT})\sin(\theta)\cos(\phi) + \cos(i_{RAT})\cos(\theta), \tag{3a}$$

where ϕ is the angle in real (3-D) space between the straight-line profile as projected onto the RHCP and the direction to the Sun as projected onto the same plane.

[24] If $\phi \neq 0$, then $i_{min} \neq 0$ and i_{min} can be calculated by

$$\cos(i_{min}) = \frac{\left(\sin^2 i_{RAT}\cos^2\phi + \cos^2 i_{RAT}\right)\cos\left(\tan^{-1}\left(\tan i_{RAT}\cos\phi\right)\right)}{\cos(i_{RAT})} \tag{3b}$$

[25] 3. Determine the local facet tilt angles: The cosines of the incidence angles as found by Lambert's law along the straight-line profile are converted into local tilt angles (θ) by inversion of formula (3a). In the general case of $\phi \neq 0$, θ can only be found numerically. However, if $\phi = 0$, formula (3a) simplifies to $\cos(i) = \cos(i_{RAT} - \theta)$. In any case the suite of slope angles obtained is not a unique transform of the radiance profile. In particular, if $\phi = 0$ then formula (3a) can be solved as $\theta = i_{RAT} \pm i$. Here the selection of the correct sign is guided by the assumption that the magnetic particle accumulation must be dome-shaped.

[26] 4. Determine the topographic profile: Once the local slope angles have been obtained, local stairs and stair heights can be associated to each pixel. The elevation can then be calculated pixel by pixel as the sum over neighbor-pixel stairs. The profile is first obtained in units "px" and can then be converted into "mm," using the resolution (calculated in mm px^{-1}) at the target. Obviously, the topographic profile determined in this way can be shifted up and down by an arbitrary additive constant, and the new profile would still satisfy the observed radiance.

[27] Above we mentioned some uncertainty on the maximum value (i_{max}) of the local incidence angle: As long as the analyzed data span over roughly the entire magnetic particle accumulation, we can reasonably require the calculated topographic profile to end approximately at the same relative height, as where it started from. Since the topographic profile as calculated is very sensitive to i_{max}. We can iterate the latter angle, until both heights are similar.

2.2.2. Selection of Radiance Data

[28] The images to be analyzed have been acquired on A068 and B048 as 512 times 512 pixels large subframes at full resolution. The images were scaled onboard from 12 to 8 bits per pixel by the means of a lookup table ("LUT3" [*Bell et al.*, 2006]), then compressed to effectively 2.6 bits per pixel by the ICER compression algorithm [*Maki et al.*, 2003]. After their transmission to Earth they were decompressed and the 12-bit format was restored by applying the corresponding inverse lookup table ("ILUT3" [*Bell et al.*, 2006]). The raw images were then processed to RAD calibrated images as part of the Pancam Calibration Pipeline [*Bell et al.*, 2006].

[29] From the MER SPICE kernels the A068 and B048 incidence angles (i_{RAT}) have been determined to 57.01° and 44.85°, respectively (Appendix B). The uncertainty on these numbers can amount to a fraction of a degree, depending on the accuracy of available rover tilt and IDD joint angles and on operational issues, e.g., on the activities that have been taken place since last determination of the rovers' fine attitude. The SPICE kernel values as given above have been checked and confirmed by analysis of shadows that are cast by different objects (especially grinding head and rotate brush) onto the plane of the revolve housing cap.

[30] During imaging the revolve housing cap was located about 1.0 to 1.1 m (B048) from the focal plane of the left Pancam, placing the magnets somewhat outside the range of good focus (1.5 m to infinity). Note that the bright saturated spot on the upper RAT contact ball is located slightly higher in A068 as compared to B048 (Figure 2), which illustrates the difference in incidence angle between the two images.

[31] At some point the conversion of radiometric into topographic profile involves the conversion of a length expressed in pixels into a length (or height) expressed in standardized physical units such as millimeters. For this

purpose we determine the resolution at target (denoted RES) by fitting an ellipse to the revolve housing cap. The following fit parameters have been found:

$$\text{A068}: a_{rh} = 56.30 \text{ px},\ b_{rh} = 46.56 \text{ px},\ \alpha' = 5.95^\circ$$

$$\text{B048}: a_{rh} = 57.67 \text{ px},\ b_{rh} = 43.55 \text{ px},\ \alpha' = 7.64^\circ$$

The unit length "px" is equal to the horizontal (or vertical) extension of one pixel in the image frame. The parameters a_{rh}, b_{rh} and α' denote semimajor axis, semiminor axis and tilt angle of the major ellipse axis with respect to vertical direction in the image, respectively. The tilt angle of the semimajor ellipse axis is intentionally denoted by the Greek letter (here α) followed by a "prime" in order to make it clear that this quantity refers to the image space (compare also notation section). Given the diameter of the revolve housing cap (d_{rh} = 33.4 mm) the resolutions at target vary in the range: 0.30–0.36 mm px^{-1} (A068), 0.29–0.38 mm px^{-1} (B048), where the smallest and largest values are achieved along the direction of the major and minor ellipse axis, respectively.

[32] As a next step, ellipses with the same axis ratio and same tilt angle as the revolve housing ellipse are drawn on top of the material accumulated on the RAT magnets (below referred to as RAT magnet ellipses). Here we assume that the area covered by magnetic rock particles is circular, just like the revolve housing cap. The following ellipse parameters have been found:

$$\text{A068}: a = 9.43 \text{ px},\ b = 7.80 \text{ px},\ \alpha' = 5.95^\circ$$

$$\text{B048}: a = 7.58 \text{ px},\ b = 5.72 \text{ px},\ \alpha' = 7.64^\circ$$

Finally, the straight-line profiles to be converted into topographic profiles are drawn across the A068 and B048 RAT magnet ellipses (Figures 5a and 5c). These profiles are forced to intersect the corresponding ellipse center. Their orientation is characterized by a tilt angle (noted β'), which is measured between that profile and the vertical direction in the image. Ideally, these pixel profiles should be oriented along the direction of the incident sunlight as projected onto the revolve housing cap in order to maximize the radiometric gradient across the particle accumulation. While this was done in the case of B048 (with $\beta' = 41.75^\circ$), the A068 straight-line profile was tilted by 20° CCW in image space (angle from hereon referred to as ϕ') off this preferred direction due to the shadow from the grinding head (resulting in $\beta' = 39.41^\circ$). The radiances across both profiles (including the artificial ellipse borders for reference) are plotted in Figures 5b and 5d. The resolution along these two particular profiles can be computed by using a standard ellipse formula:

$$\text{RES} = \frac{d_{rh}[\text{mm}]}{2r_{rh}[\text{px}]} \qquad \text{with} \qquad d_{rh} = 33.4 \text{ mm},$$
$$r = \frac{a_{rh} b_{rh}}{\sqrt{a_{rh}^2 - \left(a_{rh}^2 - b_{rh}^2\right)\cos^2(\alpha' - \beta')}}. \tag{4}$$

The resolution (RES) must depend on the distance from target to camera. This dependence is hidden in the ellipse parameters (a_{rh}, b_{rh}). From equation (4) we obtain the following resolutions:

$$\text{RES} = 0.317 \text{ mm px}^{-1}(\text{A068}),\ \text{RES} = 0.322 \text{ mm px}^{-1}(\text{B048}).$$

The ellipse parameters (a_{rh}, b_{rh}) can also be used for calculation of the emission angles: $e_{RAT} = \arccos(b_{rh}/a_{rh})$ = 36.3° (A068) and 41.4° (B048), which in turn compare reasonably well with the ones derived from the SPICE kernels (A068, 33.15°; B048, 41.89°).

[33] The above described model does not include any form of two-layer reflectance. Thus formula (1) only applies to regions where the magnetic particle accumulation is sufficiently thick. The layer thickness that effectively controls the reflectance of light may be estimated by the following formula [*Hapke*, 1993]:

$$h^* = \frac{D}{f}\frac{1+r}{1-r}, \tag{5}$$

where D is the average particle diameter, F is the filling factor of the particulate material and r is the diffuse reflectance. The filling factor increases with decreasing porosity. In practice, it ranges from 5% for loosely accumulated submicron dust particles to about 50% for sand-sized particles. The diffuse reflectance is in the range 5 to 10%. With D $\sim$ 10 μm, F $\sim$ 10% and r $\sim$ 10%, we find $h^* \sim 0.1$ mm. Although this result holds only within an order of magnitude, we keep in mind that the Lambert parameters may change, when the layer thickness of abraded rock particles drops below that value.

[34] The selected radiance profiles (Figure 5) depend linearly on the row number. On the basis of our radiometric model (equation (1)) this fact implies that the cosine of the local solar incidence angle also varies linearly with row number, which provides immediate constraints on the shape of the topographic profile. It is quite obvious that formula (1) cannot describe the radiance across the entire magnetic particle accumulation. As soon as the layer thickness drops below some critical value, the reflectance of light by the underlying surface becomes important. This critical thickness is not well known but might be of the order of 0.1 mm as demonstrated above. As a result, only some large "middle part" of the radiance profile can be used to infer the topographic profile, and this middle part is assumed to be the region, where the above described linearity is observed.

2.2.3. Conversion of Radiance Data Into Topographic Data

[35] Given the sets of radiance data, the topographic profiles are obtained as described in section 2.2.1. The model parameters and results (Table 2) are briefly discussed in this section.

[36] The Lambert parameters A_L are well within the range of shadow radiance levels measured elsewhere on the RHCP (A068, 0.002–0.003; B048, 0.005–0.007 W m^{-2} nm^{-1} sr^{-1}), as expected. The parameters B_L are similar for A068 and B048. This result is consistent with the differences in dust optical depths observed at both sites (A068, $\tau \sim 0.7$; B048, $\tau \sim 0.8$ [*Lemmon et al.*, 2004]) taking into

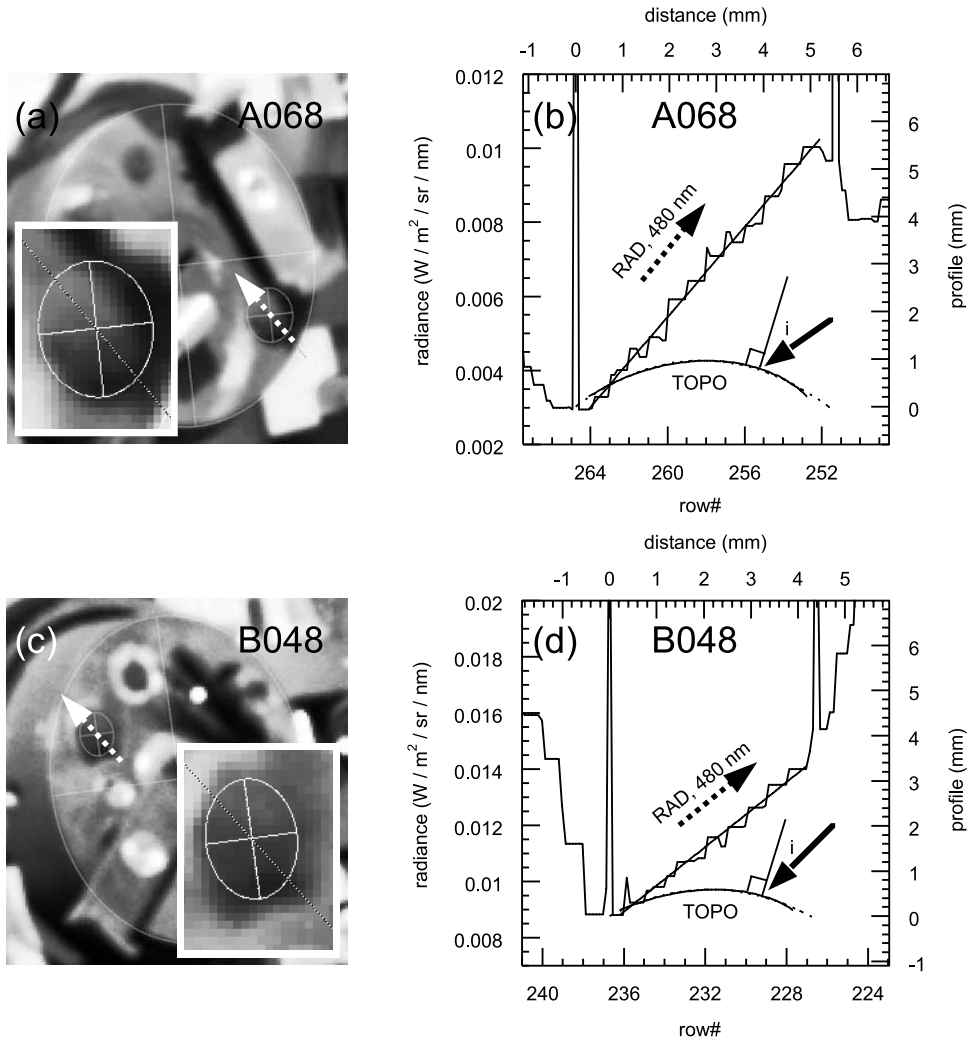

Figure 5. Conversion of radiometric into topographic profiles for the particle accumulation on RAT magnet 1_3. (a) A068, image (480 nm) with pixels of interest marked by a white stippled arrow. Note large and small ellipses fitted to RAT revolve housing cap plane and RAT magnets, respectively. Both ellipses have same tilt and same axis ratio. (b) A068, radiometric profile (left ordinate) across the pixels that are marked by the stippled arrow in the bitmap image to the left. The two artificial peaks indicate the location of the fitted ellipse. The inferred topographic profile is drawn as a solid line with no vertical/horizontal distortion (top abscissa and right ordinate). The incident sunlight is represented by a thick arrow that has the approximately correct tilt angle (i_{RAT}) within the millimeter coordinate system (top abscissa and right ordinate). The radiance increases as the local solar incidence angle (i) decreases across the particle accumulation. The dotted lines near either end of the topographic profile are an extrapolation of that profile by the means of a second-order polynomial fit. (c) Similar to Figure 5a but for B048. (d) Similar to Figure 5b but for B048. The topographic profiles in Figures 5b and 5d are drawn to the same scale. It can be seen that the B048 particle accumulation is noticeably smaller than the A068 one.

account the lower solar elevation for the A068 image as compared to B048.

[37] The inferred maximum local solar incidence angle is 85° and 68° for A068 and B048, respectively. Thus the A068 magnetic particle accumulation does almost cast a true shadow, contrary to the B048 one. In fact, the shadow extends over more than two pixels in the case of A068 and the minimum value of the analyzed straight-line profile is about 0.0030 W m^{-2} nm^{-1} sr^{-1}, i.e., in the upper range of the typical shadow radiances observed (0.002–0.003 W m^{-2} nm^{-1} sr^{-1}). Thus the maximum local solar incidence angle should indeed be very close to (or even reach) 90°. However, since the straight-line pixel profile was turned by $\phi' = 20°$ off the direction of solar incidence as projected onto the RHCP (section 2.2.2), the maximum value for the local solar incidence drops somewhat below 90°. As to B048, some kind a half shadow (Figure 5d) extends over about one pixel. The minimum radiance of the analyzed straight-line pixel profile is about 0.0088 W m^{-2} nm^{-1} sr^{-1}, thus noticeably larger than the overall shadow radiances observed (0.005–0.007 W m^{-2} nm^{-1} sr^{-1}). This fact points to a maximum value for the local solar incidence angle that

Table 2. Model Parameters and Results[a]

	Radiometric Modeling			Magnetic Particle Accumulation			
Rover and Sol	A_L, W m^{-2} nm^{-1} sr^{-1}	B_L, W m^{-2} nm^{-1} sr^{-1}	i, deg	Offset, mm	Height, mm	HDB, mm	Volume, mm^3
A068	0.00224846	0.00808026	20.1–85.0	0.0	0.75	2.3577	6.58
				0.22	0.97	2.6994	11.3
B048	0.00583904	0.00791299	5.95–68.0	0.0	0.46	1.8709	2.64
				0.13	0.59	2.1587	4.65

[a] A_L and B_L are the Lambert parameters as defined by equation (1). The offset denotes the uplift of the entire topographic profile needed for a reasonable match of the RAT magnet ellipse borders. HDB is the half diameter at base.

is considerably below 90°, and in fact, we infer a maximum solar incidence angle of only 68° ± 1°.

[38] The distribution of radiance levels at (and nearby) the B048 RAT magnet particle accumulation is somewhat complex. We note two dark lobes (one at the approximate 4 o'clock and the other on at the 6 o'clock position) below that particle accumulation (insets in Figures 2b and 5b). In fact the explanation of these dark lobes is straight forward (Figure 6): Our straight-line pixel profile is oriented along the direction of solar incidence (based on the SPICE kernels). Thus the dark lobe at the 4 o'clock position is caused by shadowing of direct solar light. However, the lobe at the 6 o'clock position is caused by shadowing of specularly reflected light from the upper RAT contact ball. As a result the B048 RAT magnet particle accumulation is illuminated by the Sun and by a secondary light source. The specularly reflected light hits the magnetic particle accumulation at a grazing angle and creates therefore a longer shadow than the direct solar light. Although the effect of the reflected light from the RAT contact ball seems to be dramatic (in particular in stretched images), it can only enhance the radiance caused by direct solar insolation by less than 20%. Fortunately, the direction of the direct solar incidence is far off the direction of incidence of this scattered light component, which allows us to separate between both contributions.

[39] The parameters in Table 2 that remain to be discussed refer to the calculated topographic profile. As pointed out earlier, these profiles are fixed in shape but can, in principle, be shifted up and down by an arbitrary additive constant. We also explained in section 2.2.2 that only some large "middle part" of the radiance profile can be inverted in terms of topography. Therefore it makes sense to uplift the entire topographic profile by a constant value (termed "offset") and extrapolate it on either side by the means of a second-order polynomial fit. The offset is chosen such that the extrapolated topographic profile is zero at the shadow border of the RAT magnet ellipse. The match between the upper (sunlit) border of the inferred topographic profile and the one of the RAT magnet ellipse can then be used as a check for the entire calculation. For both A068 and B048 we get an agreement of better than 0.5 px (Figures 5b and 5d), which is certainly acceptable taking into account the uncertainty of the location of these ellipse borders (also typically 0.5 px).

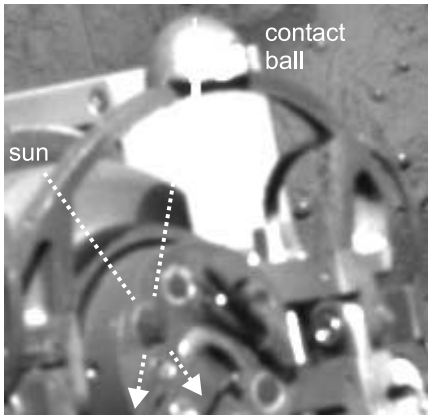

Figure 6. Illumination of the B048 RAT magnet 1_3 by the Sun and the upper RAT contact ball. The straight-line pixel profile analyzed (Figure 5c) is oriented along the direction to the Sun.

[40] With the Lambert parameters given in Table 2 and including the offset, the height of the magnetic particle accumulation is determined to 1.0 ± 0.1 mm (A068) and 0.6 ± 0.1 mm (B048). Using the inferred topography (Figure 5), dividing it up into a number of horizontal slices, and assuming rotational symmetry (slice by slice), the volume of the magnetic particle accumulation has been calculated in mm^3 (Table 2). The half diameter at the base of the particle accumulation turns out to be substantially larger than its height. Thus these particle accumulations are substantially flattened as compared to hemispherical shape. For the conclusions to be drawn later, it is important to take the parameters of the grinding process (Table 3) into consideration: The cumulated grind depth was almost three times larger on B048 as compared to A068, while the cumulated grind duration was comparable. As a result the grind rate (defined as the ratio of grind depth to grind duration) was more than three times larger on B048 than on A068 illustrating the difference in rock hardness at both sites.

[41] The uncertainties on height and volume of the particle accumulations are estimated to be in the range 10–20% and should account for the errors that are associated to the method applied here, such as the ones caused by the inaccuracy of input parameters (e.g., solar incidence angle, resolution at target) and the inherent weakness of the Lambert law that assumes the reflectance to be independent of emission and phase angle. Additional uncertainty may arise from image compression and defocus. However, the images are of fairly high quality with a compression rate of only 3.1 (resulting in effectively 2.6 bits per pixel) and we do not expect alteration

Table 3. Grind Parameters

	Cumulated Grind Depth δ, mm	Cumulated Grind Time τ		Grind Rate $v_g = \delta/\tau$, mm h^{-1}
		Hours	Minutes	
Adirondack, Humphrey (A068)	4.8	6	50	0.70
Eagle crater outcrops (B048)	12.3	5	49	2.11

of the results due to image compression, especially in rather homogeneous regions (like the RAT magnets) that do not contain sharp edges (sudden jumps in signal). As noted earlier, the images are somewhat out of focus and the pixel defocus amounts to 4 ~ 5 pixels. In fact, the mixup of pixels due to defocus may well have attenuated the gradient in signal across the RAT magnet particle accumulation, and may have altered the above reached estimate on its thickness. Fortunately, this source of uncertainty is limited, since the particle accumulation is substantially wider (~17 pixels for A068, ~13 pixels for B048) than the extension of the pixel defocus. In addition, the defocus is a systematic error that should have a roughly equal effect on both results (A068, B048). The important conclusions to be drawn in this paper (compare remainder of the present section) are based on a comparison of B048 to A068 and should therefore not be sensitive to the error caused by the defocus.

2.2.4. Implications for the Magnetization of Eagle Crater Outcrops

[42] Let us first use APXS and Mössbauer data to estimate the magnetization of Humphrey: About 17.9 wt % FeO (13.9 wt % Fe) have been found in the Humphrey RAT hole by APXS [*Gellert et al.*, 2004] and about 11% of these iron atoms belong to magnetite [*Morris et al.*, 2006a]. From these results the magnetization of Humphrey can be calculated:

$$\begin{aligned}\sigma_s(\text{Humphrey}) &= f_{Fe/tot} \cdot MBAR_{magnetite} \cdot \frac{M_{magnetite}}{3 \cdot M_{Fe}} \cdot \sigma_{s,magnetite} \\ &= 0.139 \times 0.11 \times 1.382 \times 90 \text{ A m}^2 \text{ kg}^{-1} \\ &= 1.90 \text{ A m}^2 \text{ kg}^{-1}, \end{aligned} \quad (6)$$

where F is a dimensionless fraction, MBAR is the Mössbauer area ratio, M is the molar weight (g mol^{-1}) and σ_s is the saturation magnetization ($\sigma_s \sim 90$ A m^2 kg^{-1} for pure, stoichiometric magnetite). In particular, $f_{Fe/tot}$ denotes the mass fraction of iron in the sample as provided by APXS. The magnetization obtained by (6) implies ~2.1 wt % magnetite in Humphrey.

[43] Table 3 allows a comparison of grindings at the Gusev and Meridiani sites. The grinding time has been rather similar in both cases (6 hours 50 min for A068, 5 hours 49 min for B048, summing up over all previous RAT activities up to that sol). However, the grinding depth was very different: 4.8 mm (A068) and 12.3 mm (B048), again summing over all RAT activities up to that sol. Assuming that the selection and capture efficiency for magnetic grains during rock abrasion is similar on both sites, we would expect the following magnetization for Flatrock/MER-B (hereinafter used as a generic term for the McKittrick-Flatrock group):

$$\begin{aligned}\sigma_s(\text{Flatrock}) &= \frac{v_{Flatrock}}{v_{Humphrey}} \frac{\delta_{Humphrey}}{\delta_{Flatrock}} \sigma_{s,Humphrey} \\ &= (4.6/11.3) \times (4.8/12.3) \times 1.90 \text{ A m}^2 \text{ kg}^{-1} \\ &= 0.30 \pm 0.05 \text{ A m}^2 \text{ kg}^{-1} \end{aligned} \quad (7)$$

Hence Flatrock would have a saturation magnetization that is comparable to the one of pure crystalline hematite (above Morin transition). Here we used the RAT magnet particle volumes that do include the offset that was discussed in section 2.2.3 (Table 2). However, the corresponding volumes that do not include this offset would lead to virtually the same result. Formula (7) assumes a linear relationship between saturation magnetization and capture rate and thereby volume of the magnetic particle accumulation. This indeed questionable assumption will be readdressed in section 4.

[44] Flatrock contains typically 16 wt % iron oxide or 12.4 wt % Fe ($f_{Fe/tot} = 0.124$ [*Rieder et al.*, 2004]). On the basis of Mössbauer data [*Klingelhöfer et al.*, 2004] the iron atoms (mostly ferric ions) are shared among hematite (38% MBAR), jarosite (22% MBAR), some unidentified ferric mineral (25% MBAR) as well as pyroxene (14% MBAR), the latter mineral hosting ferrous ions. If the magnetization of Flatrock was purely caused by macroscopic hematite (above Morin transition, $\sigma_s \sim 0.4$ A m^2 kg^{-1}), we would expect

$$\begin{aligned}\sigma_{s,calculated}(\text{Flatrock}) &= f_{Fe/tot} MBAR_{hematite} \frac{M_{hematite}}{2M_{Fe}} \sigma_{s,hematite} \\ &= 0.124 \times 0.38 \times 1.430 \times 0.4 \text{ A m}^2 \text{ kg}^{-1} \\ &= 0.027 \text{ A m}^2 \text{ kg}^{-1}, \end{aligned} \quad (8)$$

We can see that the saturation magnetization as calculated from APXS and MB data would be 11 times smaller than the one inferred from the RAT magnet experiment. This factor would become even larger if we allowed for some fraction of hematite to be ideally antiferromagnetic (i.e., below Morin transition). Again, the above found saturation magnetization for Flatrock (0.30 A m^2 kg^{-1}) is at best a working hypothesis that would require a perfect similarity of RAT magnet particles on both rovers in terms of magnetic hysteresis properties (compare section 4 of the present paper). Yet the fact that these two numbers are apart from each other by more than one order of magnitude suggests the presence of an additional ferrimagnetic phase that has not been identified by MB spectroscopy. In the following we will briefly discuss the potential implications of the saturation magnetization as determined above (0.30 A m^2 kg^{-1}) in terms of MB spectroscopy.

[45] If the strongly magnetic phase in Flatrock was pure magnetite, then this magnetization would translate into an abundance of 0.33 ± 0.05 wt % magnetite in the outcrop. Assuming that one single mineral can account for the observed magnetization, we can calculate the MB area ratio to be expected:

$$\begin{aligned}MBAR(\%) &= \frac{\text{nb. of Fe in fmp}}{\text{tot. nb. of Fe}} = \frac{f_{Fe(fmp)/fmp}}{f_{Fe/tot}} f_{fmp/tot} 100\% \\ &= \frac{f_{Fe(fmp)/fmp}}{f_{Fe/tot}} \frac{\sigma_{s(Flatrock)}}{\sigma_{s(fmp)}} 100\% \end{aligned} \quad (9a)$$

As previously, the symbol "f" denotes dimensionless fractions and the abbreviation "fmp" stands for ferrimagnetic phase. For example, for magnetite the fractional amount of iron in the ferrimagnetic phase ($f_{Fe(fmp)/fmp}$) would be 0.724, and for hematite it would be 0.70. In the particular case of magnetite formula (9a) rewrites

$$MBAR \sim \frac{0.724}{0.124} \frac{0.30}{90} 100\% \sim 1.9\% \quad (9b)$$

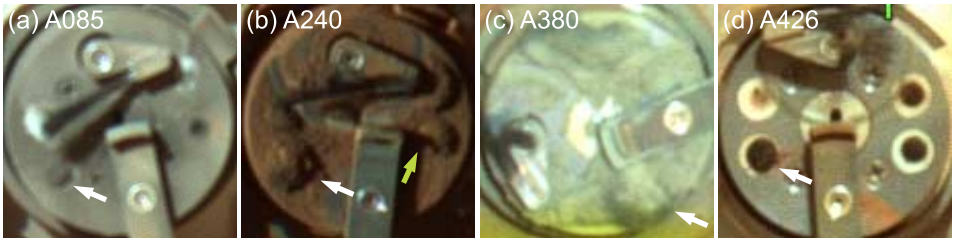

Figure 7. False color composite images (L2, L5, L7) of Spirit RAT magnets (in parentheses, cumulated grind depths achieved since acquisition of previously shown image): (a) A085 (12.7 mm), (b) A240 (21.7 mm), (c) A380 (25.9 mm), and (d) A426 (6.5 mm). The color images have been generated in a controlled way (with the RGB components stretched from 0 to 0.04 W m^{-2} sr^{-1} nm^{-1}). Note the relative changes in terms of amount, color, and texture of the material adhering to the magnets. Focus on the strong magnet 1_3 that is located next to the grinding head in the clockwise direction (white arrows). The RAT magnet particle accumulations near the rotate brush have been mechanically disturbed (most prominent in the A426 image). The dark region on RAT magnet 2 (A240, green arrow) is caused by the shadow from the grind tooth, not by mechanical disturbance of the particle accumulation.

Cation substitution would not change the MBAR significantly, as it would decrease both the saturation magnetization of the ferrimagnetic phase ($\sigma_{s(fmp)}$), and the fractional abundance of iron in that phase ($f_{Fe(fmp)/fmp}$). However, in the common case of substitution by light cations (such as Mg or Al) the saturation magnetization would decrease faster than the fractional abundance of iron, so that the above found MBAR (1.9%) may be considered as a lower bound. Pure magnetite causing such a MB signal might be detectable, whereas (fully or partially) oxidized magnetite (with similar abundance) might remain undiscovered, if the latter mineral had MB parameters similar to those of hematite. Taking into account the geochemical/mineralogical context of the site, the above suggested magnetization of Flatrock (and all other Eagle Crater outcrops) might be caused by an oxidized version of magnetite. In any case, the abraded rock material accumulated on the RAT magnets must be stained by hematite, known to be a significant part (almost 40% in terms of Mössbauer area ratio [*Klingelhöfer et al.*, 2004]) of the iron-bearing minerals in the outcrops.

3. Long-Term Accumulation of Abraded Rock Material on the RAT Magnets

[46] The accumulation of particles on the RAT magnets evolved as a result of grindings into a large variety of rocks (in particular at the Gusev site) and occasionally was affected by wind. In this chapter selected reflectance spectra of RAT magnet material will be correlated to other results (mainly Mössbauer) on the corresponding rock.

3.1. RAT Magnet Particles on Spirit

[47] Figure 7 illustrates the evolution of the Spirit RAT magnets over the first 500 sols. The strong variation in color and amount of material sticking to the magnets indicates the broad range of RAT magnet particles in terms of iron mineralogy and magnetization.

[48] Representative RAT magnet reflectance spectra across the mission are shown in Figure 8. Early in the mission, RAT magnet images were obtained after grinding on Adirondack (A035), Humphrey (A068) and Matzazal (A085). These rocks appear to belong to the same rock class [*Morris et al.*, 2006a] and the RAT magnet experiment still has the character of a monorock experiment. As mentioned in an earlier section, the material accumulated on the RAT magnets after these early grindings must be essentially magnetite-rich basalt. However, grinding of the rock is often preceded by brushing, whereby significant amounts of altered, reddish dust are lifted up. As a result, the material accumulated on the RAT magnets is generally stained by dust and their reflectance spectra (Figure 8) are not really grey, but have a significant blue-to-red slope. In Figure 8 we do not show the A035 spectrum which is of poor quality, though similar to A068. The anomalous spectrum, acquired on A240 after grinding into WoolyPatch, Clovis, and Ebenezer, may be ascribed to the presence of fair amounts of hematite and goethite in these rocks. The abraded rock material though remains rather dark, and the blue-to-red slope of the A240 spectrum is much weaker than, e.g., the

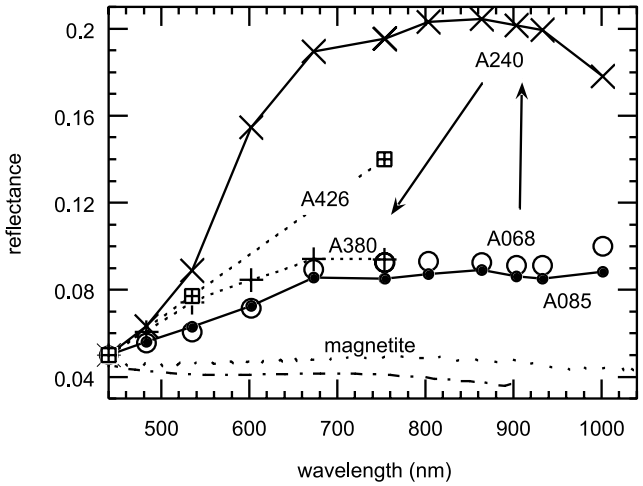

Figure 8. Reflectance spectra of Spirit RAT magnet 1_3 through several hundred sols (scaled to 5% at 440 nm). Integrating-sphere spectra of pure magnetite are also shown for reference: Synthetic magnetite (BASF 345, reflectance ~3.5 to 4%) and naturally occurring magnetite from Farmington County, Colorado (reflectance ~4 to 5%, data from spectral library version 4, http://speclab.cr.usgs.gov/spectral.lib04/spectral-lib.desc+plots.html, R. Clark, USGS).

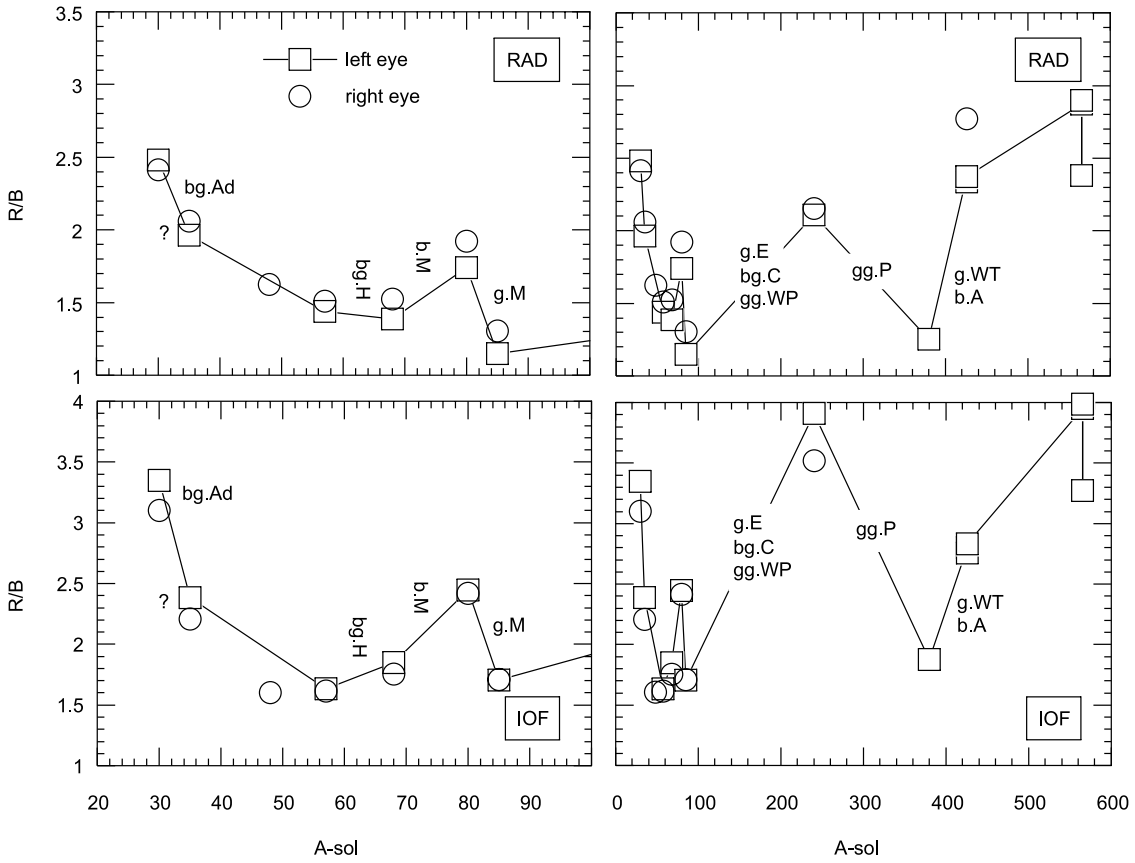

Figure 9. Red (754 nm) to blue (440 nm) ratio (R/B) versus sol number (MER-A). (top) Using RAD calibrated images. (bottom) Using IOF calibrated images. R/B refers to RAT magnet 1_3, except for A035 (1_2), A048 (1_2) and A565 (2). Selected RAT activities (b, brush; g, grind) on various rock features or targets are specified. Rock labels: Ad, Adirondack; H, Humphrey; M, Mazatzal; C, Clovis; E, Ebenezer; WP, WoolyPatch; P, Peace; A, Alligator; WT, Watchtower.

one of classic bright region spectra (Figure 3). Two of the rocks also contained significant amounts of magnetite (WoolyPatch, 15%; Ebenezer, 20% MBAR), and one notices the huge amounts of material adhering to all RAT magnets (compare A085 to A240, Figure 7). As a result, the RAT magnets likely accumulated magnetite-rich rock particles that are stained by hematite and goethite. The color is remarkably uniform across the plane of the revolve housing cap (including the RAT magnets) implying that the distribution of the coloring component (likely hematite and goethite) is not affected by the presence of the magnets. None of the reflectance spectra does exhibit the well-known spectral signatures of hematite or goethite (reflectance maxima near 600 nm and 750 nm), probably because these mineral phases are present as very small particles.

[49] On A380 huge amounts of grey material (extending even beyond the circular border of the bottom of the RAT) stick to RAT magnet 1_3 (Figure 7c). A rock named Peace was ground twice within only few sols prior to A380 to a depth of 12.9 mm (both grinds taken together) and it may not come as a surprise that the Mössbauer spectra of both grind holes showed the strongest magnetite signal (MBAR = 34%) among all rocks investigated so far (and up to A510 [cf. *Morris et al.*, 2006a]).

[50] On A426, the RAT magnets, somewhat surprisingly, appear to be cleaned up (Figure 7d). Only one single grind (A416/Watchtower rock, the last grind at the Spirit landing site due to degradation of the grinding bits) had been performed since A380. Watchtower turned out not to contain any detectable amounts of magnetite [*Morris et al.*, 2006a], and it might actually be that nonmagnetic particles liberated during grinding did kick off weakly bound particles from the magnets. However, in the period A416–A418, and very close in time to the grind activity at Watchtower (A416), strong wind gusts were identified by Pancam imaging of its calibration target [*Kinch et al.*, 2007], a series of rocks, and of the large magnets that are mounted on the rover deck in front of the camera mast [*Madsen et al.*, 2003; *Bell et al.*, 2006]. More importantly, the power budget of the rover increased by more than 50% within only few sols (A416–A420) due to clean up of the solar panels. The robotic arm was likely unstowed and the RAT magnets may have been well exposed to atmospheric activity, while some of these events occurred. We therefore suggest that these wind gusts did remove a significant part (if not most) of the weakly magnetic particles from the RAT magnets, thereby increasing the abundance of strongly magnetic (magnetite rich) particles on these magnets.

[51] In Figure 9 we summarize the evolution of the RAT magnets in terms of red-to-blue ratios (R/B ratios; red = 750 nm, blue = 440 nm). The R/B ratio is presented both in terms of RAD and IOF ratios. RAD-based R/B ratios

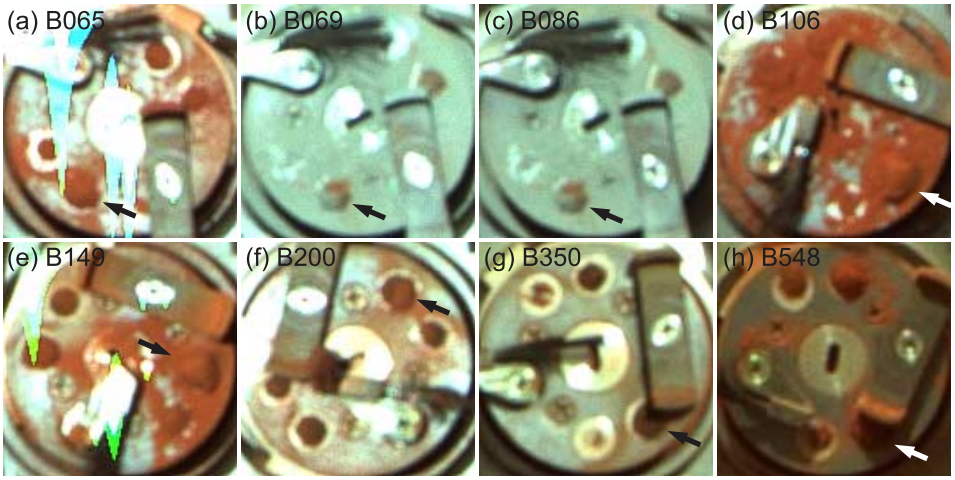

Figure 10. False color composite images (L2, L5, L7) of Opportunity RAT magnets (in parentheses: Cumulated grind depths achieved since acquisition of previously shown image): (a) B065 (12.3 mm), (b) B069 (6.4 mm), (c) B086 (0 mm), (d) B106 (7.2 mm). (e) B149 (27.0 mm), (f) B200 (43.9 mm), (g) B350 (15.7 mm), (h) B548 (12.0 mm). The color images have been generated in a controlled way (with the RGB components stretched from 0 to 0.07 W m^{-2} sr^{-1} nm^{-1}). Image B548 is darker than the others due to glancing incidence. Some of these images, in particular B065 and B149, suffer from local saturation and flow of charges to neighboring pixels [*Bell et al.*, 2003]. Note relative changes over time on magnet 1_3 (arrows), in particular the gradual cleanup of RAT magnets during operation in Endurance Crater (e, f, g). Small differences between B069 and B086 are ascribed to airborne dust and/or arm motion. The B548 image (h) is further discussed in Appendix C.

depend on the contribution from diffuse skylight relative to direct sunlight, thus on the local solar time (LST). The IOF based R/B ratio is, ideally, independent of LST but relies on the model for the dust contamination of the calibration target as well as, to a minor degree, on the tilt of the RAT centerline with respect to the Pancam calibration target (compare Appendix C). These diagrams illustrate the spectral variation of RAT magnet particles across the mission (R/B is confined in the range 1–4) and specify the impact of particular rock grinds on these spectra, as discussed in this section.

3.2. RAT Magnet Particles on Opportunity

[52] Figure 10 presents some images that illustrate the evolution of the Opportunity RAT magnets within the first 600 sols. Disregarding the images acquired on B069 and B086 (Figures 10b and 10c, to be further discussed below) the RAT magnets generally appear to be reddish, while the amount of material on these magnets changes significantly over time, demonstrating again the truly dynamic nature of the RAT magnet experiment.

[53] Some representative RAT magnet reflectance spectra are compiled in Figures 11 and 12. After early grindings in Eagle Crater outcrops (prior to B048) a milestone was the grinding into Bounce rock. Spectra acquired before (B065) and after (B069) that grinding activity are shown in Figure 11. Bounce rock is essentially composed of pyroxene and plagioclase, the first mentioned mineral being the only iron-bearing phase detectable by Mössbauer spectroscopy. Contrary to Eagle Crater outcrops, the RAT magnet experiment is now fully inline with the results from Mössbauer spectroscopy: No strongly magnetic (ferrimagnetic) phase seems to be present in that rock. The grinding process may even have removed material from the strong RAT magnet. The reddish material from grinding in Eagle Crater has been covered by a grey layer of variable thickness. At some points the underlying material is shining through. The overall uniformity of this layer indicates that the distribution of abraded rock material on the revolve housing cap is not affected by the magnets. Given the transition from a red reflectance spectrum to a grey one (Figure 11), Bounce rock does not seem to contain ferric oxides in any appreciable amount.

[54] Two image cubes (B069, B086) were acquired after grinding into Bounce rock with no RAT activity in between. The close similarity of images (Figures 10b and 10c) and spectra (Figure 11) suggests that no particles (grey or red, with varying magnetization) fell off as a result of robotic arm or rover motion.

[55] The evolution of the RAT magnets after B086 is summarized in Figure 12, where we also show some representative Eagle crater spectra for reference. Grinding into outcrop near the rim of Fram crater turned the RAT magnets red again and the spectra (B106) are rather similar to Eagle crater spectra with a blue-to-red slope almost as strong as in the B035 spectrum (Guadalupe).

[56] RAT magnet observations on B149, B200, and B350 mainly reflect grinding activities in Endurance crater: The amount of RAT magnet material on B200 remains small as compared to A240 and A380. More important here, it does not appear to be larger than the one generated prior to B048, and this despite 13 grinds in Endurance crater (conducted in the timeframe B097–B194) versus only 3 grinds in Eagle crater. Accordingly, the cumulated grind depth achieved in Endurance crater has been almost six times larger than in Eagle crater. The amount of material on the magnets did apparently reach steady state. This observation may imply an upper bound to the magnetization of the adherent

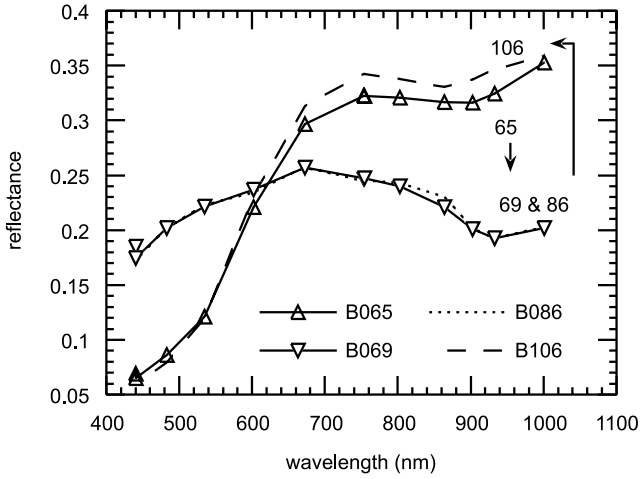

Figure 11. Reflectance spectra of RAT magnet 1_3 (MER-B) before and after grinding into Bounce rock on B066. The B069 and B086 spectra refer to gray rock material that partially covers the previously accumulated reddish outcrop material (see black arrow in Figures 10b and 10c). The data shown have been directly read from IOF calibrated images.

particles or may be explained by the particular wind regime inside Endurance crater that was observed to favor dust removal from the Pancam calibration target [*Kinch et al.*, 2007]. The spectra are similar to (and fully within the range of) Eagle Crater spectra, besides a weak dip near 860 nm (often referred to as absorption feature of poorly crystallized ferric oxides), which can be seen in the RAT magnet spectra of Eagle/Fram crater, but seems to be absent in the corresponding spectra of Endurance Crater (Figure 12). Finally, three grinds with a total grind depth of 15.7 mm have been performed in the timeframe B200–B311, followed by a brush action on Heatshield Rock on B349. Such a small number of RAT activities over a period of 150 sols explain the small amount of material on the RAT magnets as observed on B350: Material has been continuously removed by wind, while not much new material has been added. As a result, the RAT magnet material has become a concentrate of strongly magnetic material (likely dominated by magnetite or some variant of that mineral). RAT magnet images/spectra acquired at a much later time (B548) during the mission show, once more, the transition from a grayish-reddish to a distinctly red spectrum, likely caused by the grinding into a particularly soft outcrop named IceCream (B545, 6.0 mm).

[57] We summarize as follows: Spectra B149 and B200 as well as B548 are within the range of spectra acquired early in the mission in Eagle Crater (disregarding a possible weak feature near 860 nm). The dark spectrum of B350 is explained by a rather evolved, wind-controlled selection of strongly magnetic grains. We conclude that the RAT magnets remain an active tool to monitor the abundance of strongly magnetic phases in rocks. As in section 3.1, we can show the evolution of the RAT magnets in terms of red-to-blue ratios (reflectance at 750 nm divided by the one at 440 nm, inferred from either RAD or IOF-calibrated images; compare Figure 13). Disregarding Bounce rock, these ratios are in the range 1–4 and 3–7 for Spirit and Opportunity RAT magnet material, respectively. The Opportunity ratios are generally higher and more uniform over time than the Spirit ones illustrating the higher abundance of red ferric oxides in Meridiani outcrops and the lower diversity of these outcrops in terms of iron mineralogy.

4. RAT Magnet Simulations in the Laboratory

[58] In this section we will describe RAT magnet simulation experiments performed on terrestrial samples. These experiments are needed to support or refine some of the assertions made earlier in the present paper.

4.1. Analogue Samples

[59] Prior to the mission a set of magnetic reference samples were selected for simulation experiments. The geologic context of some of these samples is not known in detail. The set of magnetic reference samples was selected to meet the following requirements: (1) Cover a large range of magnetic properties, (2) include minerals that might be the cause of the magnetic anomalies on Mars, and (3) include mineral assemblages that could be a starting point for the soil-forming processes on Mars. The list of samples includes three different basalts, a picrite basalt (60 Ma) from Vaigat, West Greenland [*Larsen and Pedersen*, 2000], a volcanic rock from Rifugio Sapienza, Mount Etna, Italy and an intrusion rock (2 Ma) from an Icelandic reverse magnetic anomaly, Kjalarnes (25 km north of Reykjavik), Iceland, as well as a hematite crystal from Ouro Preto, Brazil (purchased from British Museum; see section 4.3) and a magnetite hand specimen from Ishpeming, Michigan (purchased from Ward's Inc.). The strongly magnetic phase in Vaigat and Mount Etna basalts is titanomagnetite, while the one in the Kjalarnes rock is single-domain (SD < 1 μm) incompletely oxidized titanomaghemite ($\sim$10 wt %). From hereon the three basalts will be referred to by their locality, i.e., Vaigat, Mount Etna and Kjalarnes. They have been chosen due to their widely different magnetic properties and their strongly different behavior during RAT magnet

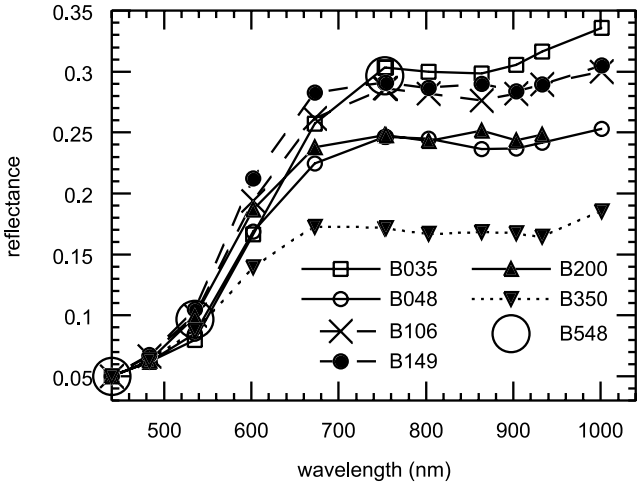

Figure 12. Reflectance spectra of Opportunity RAT magnet 1 through several hundred sols. Eagle crater data (B035, B048) are shown with same plot symbols as in Figure 3. Crosses, Fram crater. Solid circles and triangles, Endurance crater. Large open circles (only three data points), Near Erebus crater.

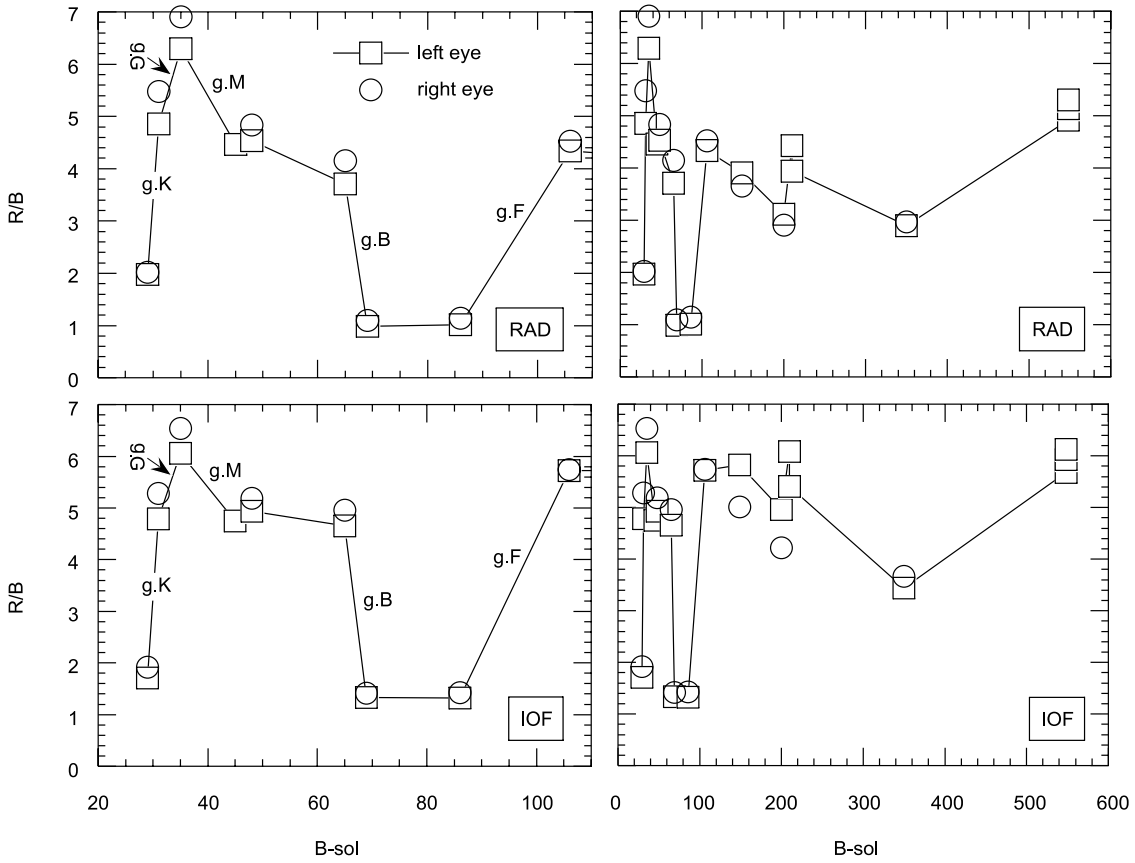

Figure 13. Red (754 nm) to blue (440 nm) ratio (R/B) versus sol number (MER-B), as inferred from (top) RAD and (bottom) IOF calibrated images (compare Figure 9 for MER-A). R/B refers to RAT magnet 1_3, except for B031, where it refers to 2. Selected RAT activities (b, brush; g, grind) on various rock features or targets are also specified. Rock labels: K, McKittrick; G, Guadalupe; M, Mojo (group of targets on Flatrock); B, Bounce rock; F, Fram crater.

simulations. Mount Etna may serve as a reasonable analogue in terms of magnetic properties, although the saturation magnetization of Mount Etna (1.42 A m^2 kg^{-1}, compare section 4.2) is somewhat lower than the one of many other rocks (including Humphrey) that have been investigated at Gusev crater [*Morris et al.*, 2006a].

4.2. Terrestrial Basalts

[60] This section is a description of selected RAT magnet simulations that have been performed at ambient pressure and temperature on some of the samples (basalts and magnetite) presented in section 4.1.

[61] Differences in temperature between Earth and Mars (typically of the order of 50°C) should not have any influence on these experiments. The difference in gravity between Earth and Mars may have some impact (compare Appendix E), but should not affect the final conclusions that are drawn from these simulation experiments. However, atmospheric pressure is an important parameter. Its effect on RAT magnet simulations will be addressed in section 4.3. The setup for simulations at ambient pressure is shown in Figure 14.

[62] As stated earlier, the three basalts behave very differently from the perspective of the RAT magnet experiment. Following observations have been made (refer to Figure 15): Vaigat basalt did not lead to strong accumulation of magnetic particles despite long grinding times (~3 h). A rather short grinding (lasting for less than 1 h) into Kjalarnes basalt generated a small magnetic particle accumulation (h ~ 0.4 mm), while a similar grinding into Mount Etna basalt generated a four times higher particle accumulation. Very brief grinding (~5 min) into magnetite using the RAT simulator (compare Appendix D) led to formation of magnetic chains extending to ~2.4 mm above the active surface of the RAT magnets (Figure 16). The results of these simulations are summarized in Table 4.

[63] Understanding these simulation experiments requires some information on the magnetic properties of the samples. Hysteresis data have been obtained for most bulk rock, RAT particles and RAT magnet particles by using a vibrat-

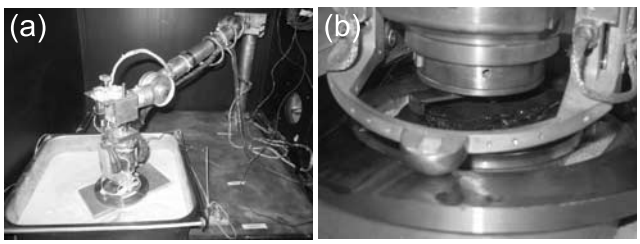

Figure 14. Setup for RAT simulation experiments: (a) Overview. (b) RAT-EM positioned on target (hematite crystal also shown in Figure 18).

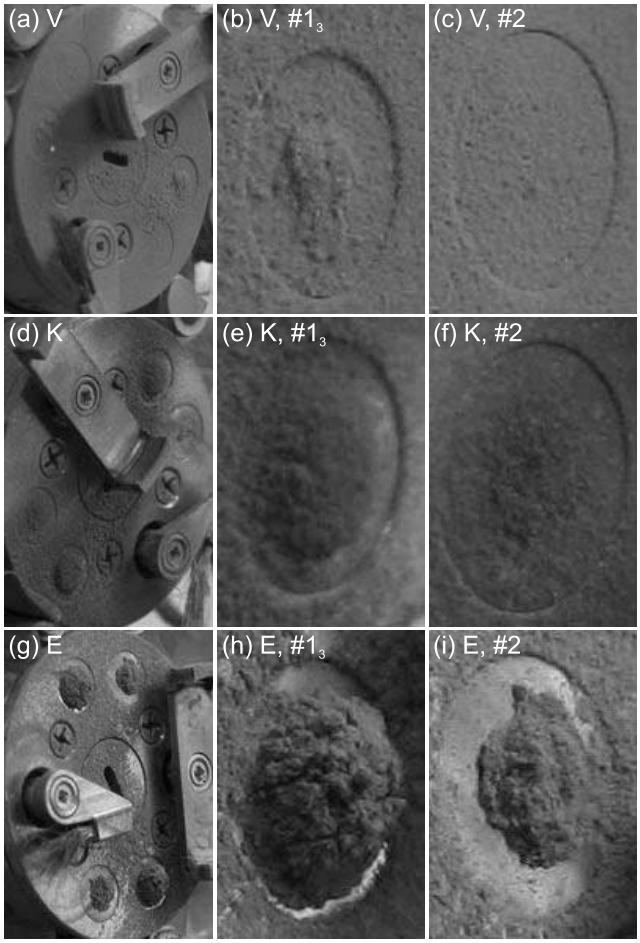

Figure 15. (a, d, g) RAT-EM grinding into terrestrial basalts. The labels V, K and E refer to Vaigat (Greenland), Kjalarnes (Iceland) and Mount Etna (Italy) respectively. (b, e, h) RAT magnet 1_3. (c, f, i) RAT magnet 2. Grind parameters and results are given in Table 4.

ing sample magnetometer. The following two empirical formulas, referred to as standard fit function (σ) and exponential fit function (σ^e), have been used to fit these data [*Gunnlaugsson et al.*, 1998]:

$$\begin{aligned}
\sigma_{\pm} &= \frac{(B \pm \mu_0 H_c)\sigma_S}{|B \pm \mu_0 H_c| + \gamma} + \frac{\chi}{\mu_0} B, \\
\frac{ds_{\pm}}{dB} &= \frac{\gamma\sigma_S}{(B \pm \mu_0 H_c + \gamma)^2 + \gamma} + \frac{\chi}{\mu_0} \gg \frac{\sigma_S}{\gamma} + \frac{\chi}{\mu_0}, \quad \text{if } B \approx \mp\mu_0 H_C, \\
\sigma^e_{\pm} &= \frac{(B \pm \mu_0 H_c)}{|B \pm \mu_0 H_c|}\sigma_S\left(1 - \exp\left[\frac{-|B \pm \mu_0 H_C|\ln(2)}{\gamma}\right]\right) + \frac{\chi}{\mu_0} B, \\
\frac{d\sigma^e_{\pm}}{dB} &= \frac{\sigma_S \ln(2)}{\gamma} \exp\left[\frac{-|B \pm \mu_0 H_C|\ln(2)}{\gamma}\right] + \frac{\chi}{\mu_0} \gg \frac{\sigma_S \ln(2)}{\gamma} + \frac{\chi}{\mu_0}, \\
&\qquad \text{if } B \approx \mp\mu_0 H_C,
\end{aligned} \tag{10}$$

where the subscript plus/minus refers to measurements with increasing (minus) or decreasing (plus) magnetic field B [T]. Most hysteresis curves could be fit with the standard fit function. However, the strong slope of the Ishpeming magnetite hysteresis near zero field required use of the exponential function. The first term of both functions describes the ferromagnetic term, and the second one describes the paramagnetic term. The complete set of fit parameters is given by the saturation magnetization σ_S [A m^2 kg^{-1}], the half saturation magnetic field γ [T] (i.e., an applied field equal to $\pm\mu_0 H_c \pm \gamma$ [T] is needed to acquire half saturation magnetization), the coercivity $\mu_0 H_c$ [T] and the high-field susceptibility χ [m^3 kg^{-1}]. Contrary to the most common terminology, the term "coercivity" refers here to $\mu_0 H_c$ [T] rather than H_c [A/m]. The experimental data and the fits are displayed in Figure 17. The various fit parameters are given in Table 5, together with the saturation remanence (σ_R) and the slope near $B = \mu_0 H_c$ (here referred to as low-field slope, $LFS \equiv \sigma_S/\gamma + \chi/\mu_0$, $LFS^e \equiv \sigma_S \cdot \ln(2)/\gamma + \chi/\mu_0$). Larger half-saturation magnetic fields imply smaller low-field slopes and vice versa. The above fit formulas work obviously best if only one type of magnetic component is present in the rock (or abraded rock). Deviations from these fits (such as wasp-shaped hysteresis curves) provide constraints on the nature of magnetic components present [*Roberts et al.*, 1995; *Tauxe et al.*, 1996; *Dunlop and Özdemir*, 1997].

[64] Let us compare parent rock, RAT particles, and RAT magnet particles in terms of their hysteresis parameters. RAT particles have larger coercivity and larger half-saturation magnetic field as compared to the rock. During rock abrasion, micron-sized particles with a very broad size distribution are generated out of bulk rock (see Appendix D). The larger fraction of single-domain magnetic grains among RAT particles explains their larger coercivity (as compared to bulk rock). RAT magnet particles must be a subgroup of RAT particles. On the basis of the hysteresis data the former particles have lower-coercivity, larger saturation magnetization, and smaller half-saturation magnetic field than the latter ones.

[65] These differences express the magnetic selection of particles by the RAT magnets. The magnetic separation is apparently less efficient for Kjalarnes as compared to Mount Etna basalt. As noted earlier, the titanomagnetite grains in Kjalarnes basalt are dominantly present as submicron-sized single-domain grains. Since RAT particles have a broad size distribution with most particles being larger than 1 μm, the particles captured by the magnets are quite similar to all other particles produced during abrasion. As a result, the selection effect is weak in the case of Kjalarnes.

[66] RAT particles and RAT magnet particles are generated from a given layer of the parent rock during a particular grind action. Therefore the hysteresis data for these two samples are a consistent data set. However, the hysteresis data for the parent rock (acquired on a millimeter-sized piece broken off the rock sample prior to grinding) may be somewhat different due to heterogeneity of the rock. Therefore care is required when comparing bulk rock to abraded rock.

[67] The magnetic hysteresis data help to better understand the above described RAT magnet simulations. RAT material from Vaigat and Mount Etna basalt has a saturation magnetization of 0.1 and 1.7 A m^2 kg^{-1}, respectively. Assuming similar capture probability of magnetic grains that are liberated during grinding, a seventeen times longer grind time (or correspondingly larger grind depth) would be needed for Vaigat (as compared to Mount Etna) to build up a magnetic particle accumulation of similar size. As a result

Figure 16. RAT simulator. (a) Top and (b) side view of the particle accumulation on magnet 1_3 after grind into magnetite (Ishpeming, Michigan). Note the formation of magnetic chains. Height of particle accumulation is ~2.4 mm.

the slow accumulation of particles is consistent with the small saturation magnetization of Vaigat basalt.

[68] Mount Etna and Kjalarnes basalts have a much larger saturation magnetization and, accordingly, much more material is accumulated on the strong RAT magnets per hour grind time (or per mm grind depth). However, it is appropriate to ask, why the accumulation of particles is so different for Kjalarnes and Mount Etna. Grinding into Mount Etna basalt generated a four times larger RAT magnet particle accumulation as compared to grinding into Kjalarnes basalt (Figures 15d–15i), and this despite the larger magnetization of the latter one.

[69] In order to go further, some fundamental comments on the particle capture process will be helpful. This complicated process can be sketched in the following way (refer to the description of the RAT magnets in section 1): Assume that a magnetic grain liberated during grinding approaches one of the strong magnets along a trajectory that is parallel to the plane of the revolve housing cap. Assume also, for simplicity, that this particle has initially no magnetic moment and no mechanical torque. The magnet provides a magnetic field of up to a few hundred mT (compare Table 1). While approaching the magnet the particle will acquire a magnetic moment depending on its distance to the magnet and on its initial susceptibility. Given a certain magnetic moment the magnetic field gradient will bend the trajectory of the particle toward the magnet. If this bending is not strong enough, the particle will just pass by the magnet instead of being trapped on its active surface. However, once a certain magnetic moment has been acquired, it needs to be realigned continuously, as the particle moves on. Here the coercivity plays an important role: If it is large, then the alignment of the magnetic moment requires a mechanical rotation of the particle. If it is small, then the magnetic alignment can be achieved either by mechanical rotation or by remagnetization. Obviously, a small coercivity favors capture of the particle on the active surface of the magnet. The coercivity turns out to be an important dynamical parameter of the capture process. The question is: What is meant by "small" and "large coercivity" in the context of the RAT magnet experiment? Here the simulation experiments guide the way.

[70] Let us return to the Mount Etna and Kjalarnes experiments. The grind depths are similar in both runs, thus a similar volume of abraded rock material has been generated during grinding. As a result, the strong difference in volume must reveal a strong difference in capture probability.

[71] Both basalts have similar half-saturation magnetic fields but very different coercivities. The saturation magnetization of Kjalarnes basalt is somewhat higher (as pointed out earlier), but this could hardly provide any explanation. On the basis of the above discussion of the capture process we explain the difference in accumulation of particles between Mount Etna and Kjalarnes basalt by their difference in coercivity (0.04 and 0.10 T, respectively, compare Table 5). During grinding into Mount Etna basalt significant amounts of magnetic particles have been accumulated on both types of magnets (Figures 15g–15i), while grinding into Kjalarnes basalt lead to accumulation of little material on magnet 1 and formation of a uniform blanket (held by electrostatic forces) on magnet 2 (Figures 15d–15f). Apparently, the accumulation of particles on the strong RAT magnet becomes increasingly difficult (and slow), when the coercivity of RAT magnet material increases beyond 0.10 T. The same applies to RAT magnet 2 with a critical value for the coercivity of ~0.05 T. Given the complexity of the capture process, these values are, almost by coincidence, close to the maximum value of $|B_x|$ (or $|B_y|$) on the active surface of both magnets (compare Table 1).

4.3. Effect of Atmospheric Pressure

[72] In this section, RAT magnet simulations performed at ambient conditions (air, 1 atm) and at Martian atmospheric conditions (CO_2, 7 mbar) will be used in order to address the effect of atmospheric pressure. Both types of simulation experiments have been performed at room temperature.

[73] The sample was a hematite crystal from Ouro Preto, Brazil. A postgrind image is shown in Figure 18. This crystal is intergrown with small amounts of magnetite. Its magnetization is therefore somewhat larger than the one expected for pure hematite (Figure 19). The abundance in magnetite is ~0.9 wt % as inferred from magnetization data (Figure 19 and Table 5), which in this particular case is still below the detection limit of Mössbauer spectroscopy [*Leer et al.*, 2006]. Here we refer to this sample by the generic term "crystal" without knowing the average extension of truly crystalline domains.

[74] The large coercivity of the abraded rock sample (~40 times larger as compared to rock, compare Figure 19 and Table 5) is consistent with the generation of hematite grains predominantly in the single domain magnetic state [*Dunlop and Özdemir*, 1997; *Kletetschka et al.*, 2000a; *Kletetschka and Wasilewski*, 2002].

Table 4. Terrestrial Basalt Grind Parameters and Results for RAT Magnet 1_3[a]

	Grinding Operation			Particle Accumulation (RAT Magnet)		
	Cumulated Grind Depth δ, mm	Cumulated Grind Duration τ	Grind Rate $v_g = \delta/\tau$, mm h^{-1}	Height h, mm	Half Diameter at Base HDB, mm	Volume v, mm^3
Vaigat, Greenland	2.09	3 hours	0.70	<0.1	1.35 ± 0.10	-
Kjalarnes, Iceland	1.42	54 min	1.58	0.4 ± 0.1	2.30 ± 0.05	<2
Mount Etna, Italy	1.68	48 min	2.10	1.7 ± 0.1	2.35 ± 0.05	19 ± 1

[a]Compare to Tables 2 and 3.

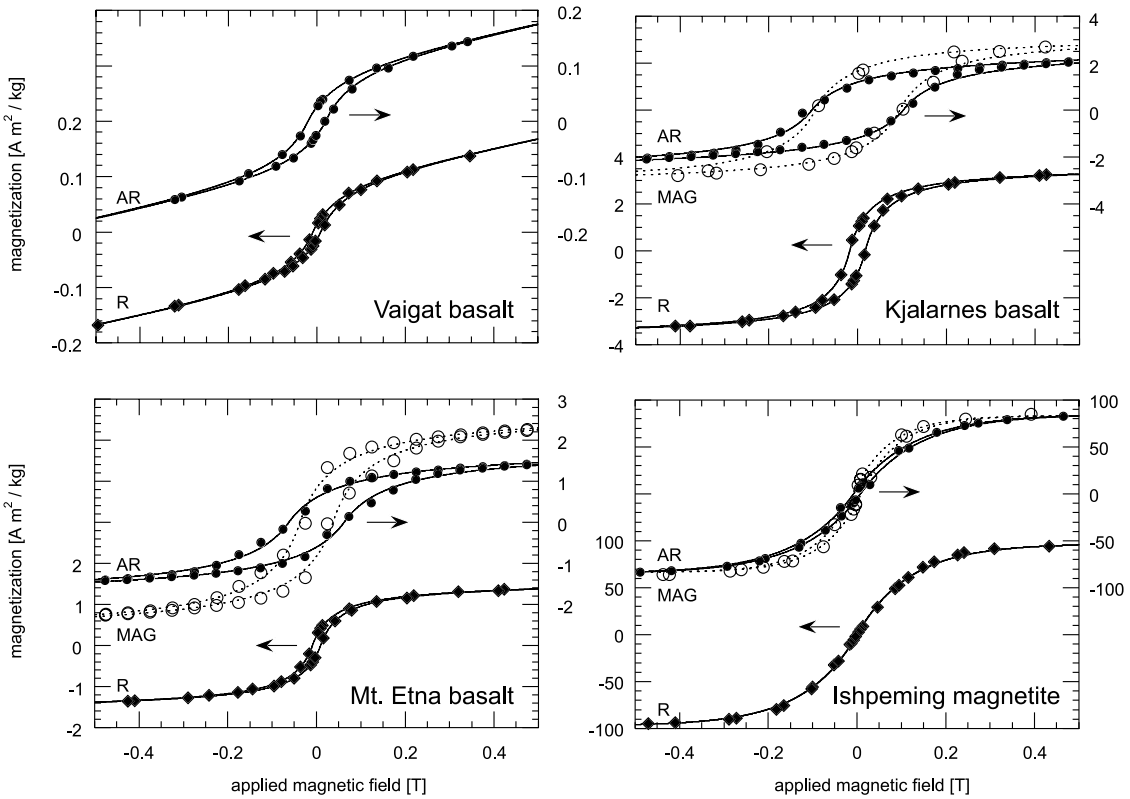

Figure 17. Magnetization of some reference samples as a function of the applied field. Left and right ordinate in each graph have same scale, such that the shapes of rock and abraded rock hysteresis curves can be compared to each other. Only shown is the range for the applied field that is relevant for the RAT magnet experiment (−0.5 to 0.5 T). All graphs have same legend but refer to different samples. Black curves show rock (R) hysteresis (refer to left ordinate), red and blue curves show hysteresis curves for abraded rock (AR) and material accumulated on magnet 1 (MAG), respectively (refer to right ordinate). The AR and MAG data presented have been acquired on material as generated by the RAT simulator (compare Appendix C), except data referring to AR/Kjalarnes, AR/Mount Etna, and MAG/Mount Etna that has been generated by the RAT-EM. Fit parameters for all hysteresis curves shown are given in Table 4.

[75] The appearance of the RAT magnets after two grindings into the crystal is shown in Figure 20. Both tests have been performed under similar conditions (grind duration 22 min, grind depth 1.0 mm), except gas pressure (1 atm versus 7 mbar) and type of gas (air versus CO_2). It can be seen that the amount of material accumulated on the magnets is larger at ambient pressure as compared to low pressure. The observation is consistent with the following physical picture: At low pressure the particles liberated during the grind process are less affected by atmospheric drag and so would have a greater tendency to be transported away from the immediate vicinity of the RAT. Only particles that are accelerated within a narrow-angle cone of appropriate orientation are captured by the magnets. However, at ambient pressure the situation is quite different: The particles produced during grinding are decelerated due to friction with the surrounding gas and remain confined within a slowly expanding dust cloud near the place where they have been created. As a result they are more likely to be captured by the magnets.

[76] The above explanation does not mention particle size in any way. At ambient pressure a dust cloud can always be seen during grinding, while such a cloud does apparently not form at low pressure. From a theoretical point of view a dust cloud may be formed in both cases, although at low pressure, only the smallest particles can be lifted up and held in suspension. These particles may not be visible to the naked eye due to a smaller light scattering cross section and/or a different angular dependence of the scattering profile.

[77] Although the initial accumulation of particles on the magnets is expected to be faster at ambient pressure as compared to low (Martian) pressure, there is no physical reason that would prevent the magnets from eventually accumulating an equal amount of material at low pressure provided sufficiently long grinding. In fact, at arbitrarily long grind times, the accumulation of particles at low pressure may even exceed the one at ambient pressure, because, given the turbulence caused by the nearby grind tool and rotate brush, weakly bound RAT magnet particles (e.g., material near the top of the magnetic particle accumulation) is expected to be easier lifted off again at ambient pressure.

[78] The material accumulated on the strong magnet (magnet 1_3) has not been studied separately. However, by comparison with other simulation experiments we expect this unit to be enriched in magnetite and to have a much narrower hysteresis loop. It is not clear why the amount of material accumulated on the weak magnet (magnet 2) is so small.

Table 5. Hysteresis Parameters for the Magnetic Reference Samples[a]

Sample	σ_S, A m^2 kg^{-1}	γ, T	$\mu_0 H_c$, T	χ, 10^{-6} m^3 kg^{-1}	σ_r, A m^2 kg^{-1}	σ_r/σ_S	μ_0LFS, 10^{-6} m^3 kg^{-1}
V1	0.101	0.061	0.0095	0.194	0.014	0.14	2.28
V4	0.111	0.075	0.0222	0.196	0.025	0.23	2.07
E1	1.42	0.046	0.0093	0.21	0.24	0.166	38
E4	1.66	0.110	0.063	0.16	0.60	0.36	19
E5	2.55	0.078	0.037	0.18	0.82	0.32	41
K1	3.49	0.047	0.0177	0.20	0.96	0.28	94
K4	2.3	0.10	0.105	0.6	1.7	0.74	37
K5	3.2	0.09	0.095	0.0	1.7	0.52	45
Is1[b]	97	0.081	0.0001	0	0.01	0.0001	1042[c]
Is4[b]	84.9	0.089	0.0077	2	4.8	0.057	829
Is5[b]	83.5	0.057	0.0095	7.1	8.7	0.104	1290
OP1	0.8	0.02	0.009	0.267	0.25	0.31	51
OP4, 1	0.39	0.81	0.39	0.171	0.13	0.33	0.78
OP4, 2	0.28	0.61	0.40	0.336	0.11	0.40	0.91

[a]The standard fit function has been used (refer to text), unless stated otherwise. The first four parameters (σ_s, γ, $\mu_0 H_c$, χ) represent a complete parameter set needed to describe the magnetic hysteresis; the remaining three parameters (σ_r, σ_r/σ_s, μ_0LFS) have been calculated. The first three parameters (σ_s, γ, $\mu_0 H_c$) are most important for the RAT magnet experiment. The low field slope (LFS) is here tabulated as μ_0LFS for easy comparison with the high-field susceptibility χ, where $\mu_0 = 4\pi \times 10^{-7}$ Vs A m^{-1} is the vacuum permeability. Acronyms for collection locality: V, Vaigat; E, Mount Etna; K, Kjalarnes; Is, Ishpeming; OP, Ouro Preto. The sample label is composed of one (basalts) or two characters (mineral samples) that specify the collection locality followed by a one-digit number: 1, 2, 3 indicating millimeter-sized piece from a certain region (labeled 1, 2, 3) inside the rock volume (assess homogeneity); 4 is RAT material (collected on/nearby the sample), and 5 is RAT material that has been accumulated on the magnets (in practice on RAT magnet 1), also referred to as RAT magnet material, subgroup of group 4.

[b]Exponential fit function used.

[c]The uncertainty is on the last digit given.

[79] Some material is bound to regions outside the magnets after grinding at ambient pressure (not at low pressure), an effect likely caused by humidity. In general the amount of nonmagnetic material bound to the revolve housing cap is small as compared to simulation experiments on basalts (section 4.2).

[80] It is not possible to quantify the difference between low- and high-pressure experiment. However, comparing the simulation experiment on Mount Etna basalt (section 4.2) to grinding into Humphrey provides a rough idea on the difference that may be observed under certain circumstances:

$$\frac{\text{dust accum.(Earth)}}{\text{dust accum.(Mars)}} = \frac{v_{Etna}/\delta_{Etna}}{v_{A068}/\delta_{A068}} = \frac{38/1.68}{48/4.8} \sim 2.3, \qquad (11)$$

where v is the volume of the magnetic particle accumulation (calculated in relative units, as in section 2.2) and δ is the grind depth (in mm). The ratio 2.3, as it is calculated here, does obviously include all differences that may exist between both environments. The difference in atmospheric pressure is believed to be most important. The difference in gravity may also have some effect (Appendix E). Finally, differences between both rocks in terms of saturation magnetisation are neglected. Taking them into account would increase this ratio to $\sim$3.

4.4. Conclusions

[81] The simulation experiments performed on hematite at low (Mars-like) and ambient pressure show that accumulation of particles on the strong magnet is faster at ambient pressure, probably by a factor of 2 or 3.

[82] From the simulation experiments performed at ambient pressure on basalts we conclude that accumulation of material on the RAT magnets requires the following two conditions to be met: (1) The liberated particles must be sufficiently magnetized given their typical kinetic energy and (2) a sufficient amount of such particles must be available. Condition 1 provides a constraint on the magnetization of the particles that come to rest on the active surface of the RAT magnet given some initial kinetic energy. Remember that the term ''kinetic energy'' is important for the interpretation of the RAT magnet experiment at Martian conditions, where the drag is weaker. It may be assumed that the average kinetic energy communicated to an individual particle is approximately the same for any grinding activity. Preload of the RAT onto the rock to be grinded as well as RAT current may well affect this kinetic energy. Yet deviations from this hypothesis simply express the semiquantitative aspect of the RAT magnet experiment.

Figure 18. Surface of the hematite crystal (Ouro Preto, Brazil) after several grinds (including the grinds described here). Note the circular tracks ($\sim$22 mm in diameter) from the grind wheel and the terraces (top of image) witnessing two preceding grinds to depths of $\sim$1 mm.

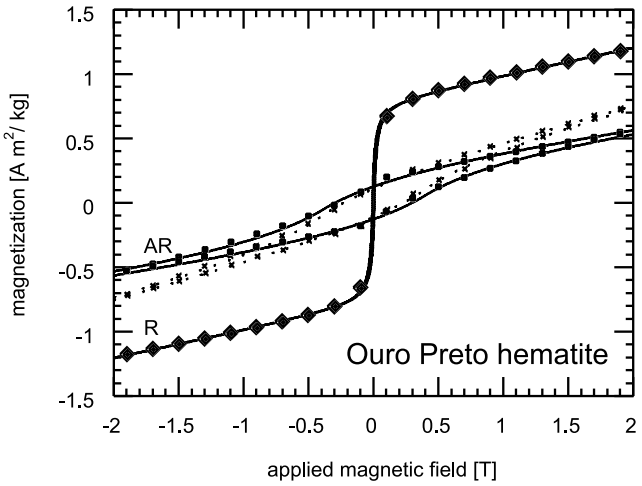

Figure 19. Magnetization of the hematite crystal (Ouro Preto, Brazil) as a function of the applied magnetic field. The saturation magnetization is somewhat larger than the one of pure hematite (macrocrystalline hematite above Morin transition) due to traces of magnetite. Different hysteresis curves have been found for the abraded material. Fit parameters for hysteresis curves are given in Table 4.

[83] Above we required that the particles should be sufficiently magnetic in order to be decelerated and captured by the magnets (given some initial kinetic energy). This constraint can be quantified in the following way: (1) Small coercivity, $\mu_0 H_C < \sim 0.10$ T (magnet 1), $\mu_0 H_C < \sim 0.05$ T (magnet 2), (2) small half-saturation magnetic field, $\gamma < 0.1$ T, and (3) substantial saturation magnetization, $\sigma_s > 0.5$ A m^2 kg^{-1}. From other simulation experiments (not described here) we know that samples with a saturation magnetization as low as 0.7 A m^2 kg^{-1} can give rise to strong accumulation of particles, if coercivity and half-saturation magnetic field are small and if such particles are readily available (see condition 2). Obviously, the above numbers may not be taken too literally and should only be considered as guidelines for the interpretation of the RAT magnet experiment. Note also that the above parameters refer to RAT magnet particles, not RAT particles. The latter unit may have large coercivity and large half-saturation magnetic field, and still substantial amounts of material may be accumulated on the magnets. However, it must contain at least one type of (easily separable) magnetic grains that meet the above requirements. Finally, it should be noted that the above requirements have been inferred from simulation experiments performed at ambient pressure. However, the given inequalities should remain valid in the low-pressure regime, where the capture of magnetic grains is more difficult due to higher flyby velocity (equivalent to shorter duration of interaction with RAT magnets, compare section 4.3).

[84] Condition 2 is a statistical constraint on the number of particles that meet the above requirements. Obviously, accumulation of particles on the RAT magnet requires that the rock represents a rich source for such particles during grinding. The number of such particles is related to the saturation magnetization of RAT material or bulk rock. Note that this quantity is approximately similar for the two types of samples (taking into account spatial heterogeneity of the rock, compare Table 5). Contrary to condition 1, we cannot specify a lower limit for the saturation magnetization that would be needed for substantial accumulation of particles on the magnets. In principle an arbitrarily low saturation magnetization could be compensated by excessively long grind times.

[85] Both points mentioned above contribute to the accumulation of material on the magnets. Many weakly magnetic or few, strongly magnetic particles may form a similar magnetic particle accumulation. Therefore we cannot estimate typical values for the magnetic properties of RAT magnet particles, but can only provide lower/upper bounds. Statements on the saturation magnetization of the bulk rock must also take grind depth (or grind time) into account.

5. Implications for Eagle Crater Outcrop: Presence of a Ferrimagnetic Phase?

[86] This section summarizes the implications of the above described radimometric analysis as well as simulation experiments for the magnetic phase of Eagle crater outcrops.

[87] 1. Referring to RAT magnet particles, the fact that magnetic grains are captured by both strong (magnet 1_3) and weak (magnet 2) RAT magnets (Figure 2) provides constraints on the magnetic properties of these grains (compare section 4): A coercivity ($\mu_0 H_C$) < 0.05 T, a half-saturation magnetic field (γ) < 0.1 T and a saturation magnetization (σ_s) > 0.5 A m^2 kg^{-1}.

[88] 2. Referring to the rock (as a whole), the abundance of the magnetic phase in the outcrop is not well constrained. In section 2.2 we adopted a saturation magnetization of

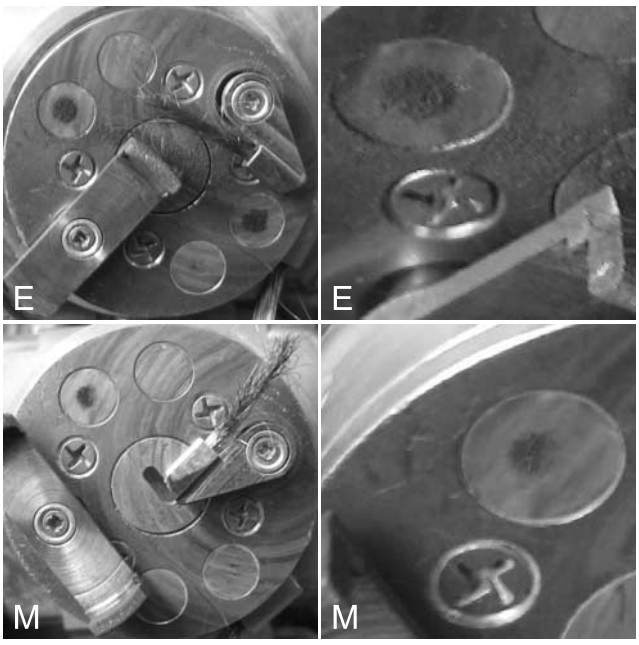

Figure 20. Simulation experiments on hematite. (top) Terrestrial ambient conditions ("E", 1 atm, air). (bottom) Martian conditions ("M", 7 mbar, CO_2). (left) Overview. (right) Detail (strong magnet 1_3 viewed obliquely). The particle accumulation on magnet 1_2 is disturbed by the brush. The amount of material captured by magnet 1_3 is substantially smaller at low pressure (bottom) as compared to high pressure (top).

0.45 A m^2 kg^{-1} as a working hypothesis. This would require a close similarity of RAT magnet particles on Spirit (A068) and Opportunity (B048) in terms of magnetic hysteresis. Obviously we do not have the data at hand that would be needed to judge on that, since the information on the characteristics of the magnetic hysteresis is incomplete (compare point 1). However, the difference in shape between the A068 and the B048 magnetic particle accumulation (section 2.1) indicates that a close similarity does not exist and it is unclear how much that would affect the postulated whole rock magnetization (0.30 A m^2 kg^{-1}), which is definitely a weak number.

[89] Referring to the conclusions drawn from the simulation experiments (compare point 1 above) the lower bound for the RAT magnet particles has been set to 0.5 A m^2 kg^{-1}, thus a value that is (almost) compatible with pure hematite. Note, however, the important point: Postulating that the RAT magnet material consists of pure hematite is equivalent to postulating that (1) the hematite grains can be perfectly separated out from the rock during the grinding process and (2) all hematite particles are in the canted ferromagnetic state above Morin transition. Point 1 seems unlikely, since the RAT magnet reflectance spectra are by no means indicative of pure hematite, but resemble much more the spectra of reddish Martian dust (Figure 3). In addition, the simulation experiments performed on Mount Etna and Kjalarnes demonstrated that a large coercivity can efficiently inhibit the accumulation of material on the RAT magnets. Noting that the hematite sample Ouro Preto has a coercivity that is four times larger than the one of Kjalarnes, it seems highly unlikely that substantial amounts of this material could be accumulated on the magnets (Figure 19 and Table 5). Also the much larger half-saturation magnetic field (Figure 19 and Table 5) works against the hematite hypothesis.

[90] If hematite was the only magnetic component in these outcrops, their saturation magnetization would amount to less than 0.03 A m^2 kg^{-1} (as pointed out earlier). On the basis of the above described simulation experiments, such a low magnetization (four times smaller than the one of Vaigat basalt) is hardly compatible with the actually observed particle accumulation on the strong magnets (B048), especially when taking into account the noticeable effect of pressure on the accumulation of magnetic particles. We would rather argue that the simulation experiment performed on Vaigat basalt provides evidence for a saturation magnetization of Eagle crater outcrop larger than 0.1 A m^2 kg^{-1}, a result that is consistent with the tentative estimate of 0.45 A m^2 kg^{-1} (section 2.2).

[91] Taking all arguments together, it is quite clear that hematite is only a marginal candidate for the Opportunity RAT magnet experiment, although the final decisive simulation experiment has not yet been performed. The strongest case for hematite and against an additional ferrimagnetic phase is that Mössbauer spectroscopy did not find such a ferrimagnetic phase in the outcrops, which, if present, may be hidden in the strong hematite signal. As a result this phase is required to have Mössbauer parameters that are very similar to the ones of hematite.

[92] The reddish color of RAT magnet material (B048) as well as the presence of substantial amounts of hematite in these outcrops [*Klingelhöfer et al.*, 2004] suggest strongly that hematite is part of the RAT magnet material (and maybe its dominant reddish pigment), but this would be due to nonmagnetic adhesion of these hematite grains to a more strongly magnetic fraction of particles that are efficiently attracted and captured by the magnets. Obviously, the coexistence of hematite and a strongly magnetic phase within these particles cannot be ruled out either.

[93] Prime candidates for a strongly magnetic phase are partially oxidized magnetite and maghemite. The high values for the ratio Fe^{3+}/Fe_{total} as inferred from MB spectra do favor some oxidized variant of magnetite, rather than pure magnetite. The presence of a magnetite-like component would not come as a surprise, since magnetite has been identified in airborne dust [*Goetz et al.*, 2005] and in basaltic soils in the Meridiani plains [*Yen et al.*, 2005; *Morris et al.*, 2006b]. Postulating the presence of an altered version of magnetite in the outcrops does not seem unreasonable, given the mineralogical and morphological evidence for the role of liquid water in the formation of these units.

[94] Pyrrhotite (Fe_7S_8), though present in SNC meteorites [*McSween*, 1985] and often proposed as a possible carrier of Martian magnetic anomalies [*Connerney et al.*, 1999; *Kletetschka et al.*, 2000b; *Rochette et al.*, 2001], should not have formed in the assumed geochemical environment that lead to the formation of the outcrops and is therefore considered to be a very remote possibility for the strongly magnetic phase.

[95] Finally, one might ask, if the material observed on the RAT magnets could be provided by other sources than the outcrop. Magnetite has been identified in basaltic soils as well as in airborne dust at both landing sites [*Yen et al.*, 2005; *Goetz et al.*, 2005]. However, these options can be ruled out: Basaltic soil has not been disturbed or stirred up prior to acquisition of the B048 RAT magnet images and settling of airborne dust out of the atmosphere is by far too slow to account for the RAT magnet particle accumulation observed early in the mission. Also, brushing of rocks generally reddens the RAT magnets without adding significant amounts of dust to their active surface. The variations in amount of RAT magnet material, which have been observed throughout both missions (Figures 7 and 10), are controlled either by grinding activities (supply of material from the interior of the ground rocks) and/or by wind.

6. Summary

[96] The RAT magnets have been a dynamic target for abraded rock material during more than 400 sols on both rovers. The spectral properties as well as the amount of material adhering to the RAT magnets changed after each grinding and are consistent with the mineralogical composition of the ground rocks, as inferred from APXS and MB spectroscopy.

[97] The dark grey material on the Spirit RAT magnets is with near-certainty identified as magnetite-rich basalt, while the reddish material on the Opportunity RAT magnets could not be identified. Comparison with simulation experiments suggests the presence of moderate amounts (<1 wt %) of a strongly ferrimagnetic phase in Meridiani outcrops, although hematite has not been proven to be unable to explain the observations. A final decision must rely on further simulation

Table A1. Selected Pancam RAT Magnet Observations[a]

Sol	Sequence	Filters	Comments
A013	p2510.07	L27, R12	specular reflections, bad signal at RM
A030	p2558.01	L23457, R127	before first G on Adirondack
A034	p2572.01	L23457, R127	after B, magnets in shadow
A035	p2576.01	L23457, R12	after G on Adirondack
A048	p2865.02	L7, R127	
A057	p2869.02	all[b]	before B on Humphrey
A068	p2139.02	all	after B and G on Humphrey
A080	p2142.02	all	after B on Mazatzal
A085	p2146.02	all	after G on Mazatzal
A240	p2133.03	all	after several B and G
A380	p2146.03	all	after several B and G, latest two consecutive G on Peace (magnetite-rich)
A426	p2580.08	L257	RAT inspection, three different orientations; after strong wind gusts and G on Watchtower (magnetite-free)
	p2581.08	L257	
	p2582.08	L257	
A565	p2134.04	L257	RAT inspection, three different orientations; similar to A426
	p2135.04	L257	
	p2136.04	L257	
B009	p2510.07	L27R12	specular reflections, bad signal at RM
B029	p2138.01	all	before G on McKittrick
B031	p2141.01	all	after G on McKittrick
B035	p2142.01	all	after G on Guadalupe
B045	p2147.01	L257R17	after G on Mojo, RM off FOV center
B048	p2131.02	all	after G on Mojo, repetition of B045
B065	p2132.02	all	before G on Bouncerock, no G since B048
B069	p2136.02	all	after G on Bouncerock
B086	p2137.02	all	before G on Fram, no B/G since B069
B106	p2142.02	all	after G on Fram
B149	p2143.02	all	after five G near rim of Endurance Crater
B200	p2132.03	all	after eight G (Endurance crater)
B210	p2137.03	L27R1	RAT diagnostic, no B/G since B200
	p2138.03	L27R1	
B350	p2140.04	all	after three G (Endurance Crater), latest on B311; after B on Heatshield Rock (B349)
B548	p2138.05	L257	after B/G on Yuri (near Vostok Crater), B401–402; after B/G on IceCream (outside Erebus), B544–B545
	p2139.05	L257	
	p2140.05	L257	

[a]Filter labels are explained in Table A2. Abbreviations are B, brushing; G, grinding; RM, RAT magnets.
[b]The term "all filters" is equivalent to L2-7 and R1-7.

experiments that need to be performed on carefully selected samples under Mars-like, environmental conditions.

Appendix A: Overview Over the RAT Magnet Experiment

[98] Table A1 lists important RAT magnet observations. Table A2 lists Pancam filter specifications and explains the filter labels. For simplicity the nominal value (440 nm) has been used for blue filter data (L7, R1) in all spectra presented in this paper.

Table A2. List of Pancam Filters[a]

λ, nm	FWHM, nm	Filter Label (LE)	Filter Label (RE)
739	338	L1 (clear)	
753	20	L2	
673	16	L3	
601	17	L4	
535	20	L5	
482	30	L6	
432	32	L7	
440	20	L8 (ND5)	
436	37		R1
754	20		R2
803	20		R3
864	17		R4
904	26		R5
934	25		R6
1009	38		R7
880	20		R8 (ND5)

[a]See *Bell et al.* [2003, 2006]. Abbreviations are LE, left eye; RE, right eye; ND, neutral density. False color RGB composite images shown in the main section are composed of L2, L5, and L7 with equal weight given to all three components.

Appendix B: Lighting and Viewing Geometry for the RAT Images, Acquired Through Filter L6 on A068 and B048

[99] The position vectors for Sun ($\hat{S}$) and left Pancam eye ($\hat{L}$) (Figure B1) are computed from the attitude data (SPICE C kernels) for the rovers and for the actuator joints of the IDD. Then the angles are calculated from the position vectors. The results are summarized in Table B1.

Appendix C: Scaling of Radiance and I/F Reflectance

[100] This appendix provides a short note on uncertainties of radiances and diffuse reflectances that are presented in this paper. A RAD calibrated image provides the absolute radiance in W m^{-2} sr^{-1} nm^{-1} [*Bell et al.*, 2006]. Obviously, the values recorded in these images depend on the relative weight of direct incident solar light and diffuse sky light, thus on the local solar time (LST) and the variability in atmospheric dust conditions, which may occur on diurnal or seasonal timescales.

[101] An IOF (also known as radiance factor) calibrated image provides the bidirectional reflectance with respect to a (normally illuminated), ideally white Lambert reflector. Data processing involves the radiance received from the Pancam calibration target (CT; data acquired close in time with the images to be calibrated). If the surface of interest (the RAT revolve housing in our case) is tilted with respect to the calibration target, the resulting radiance factors (I/F values) are inaccurate, because the lighting-viewing geometry and the relative contribution of diffuse sky light versus direct sunlight are different for both targets. To first order the radiance factors of the revolve housing (as received from the calibration pipeline) can be corrected by introducing a wavelength-independent scaling factor.

[102] The accuracy of this procedure is illustrated in the example of nine RAT diagnostic images (B548) that have been acquired through three filters (L7, L5, L2) at three

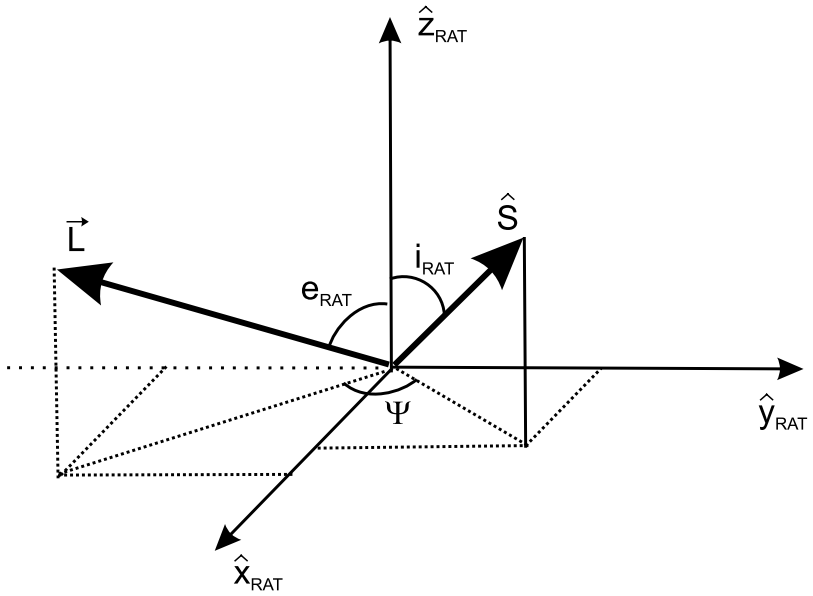

Figure B1. Vectors and angles that characterize the lighting-viewing geometry of the RAT revolve housing cap plane. The origin of the basis vectors ($\hat{x}_{RAT}$, $\hat{y}_{RAT}$, $\hat{z}_{RAT}$) is located in the center of that plane.

different IDD positions (referred to as position 1, 2 and 3) in order to assess the status of the grinding head. In these images a region of interest is selected (here sunlit part of RAT magnet 1_3; see arrows in Figure C1). It turned out that IDD position 3 provided the highest (nominal) radiance factor for this particular spot. Therefore the spectra for the two remaining positions have been scaled up by some factor to precisely match the radiance factor obtained through filter L7 (440 nm) for IDD position 1 (Figure C2). The relative deviations of the radiance factors at 754 nm provide an idea of the uncertainty to be expected. The same procedure has been applied to the radiances (Figure C2). Note that both positioning and size of region of interest are user-defined, and contribute to the deviation seen.

[103] The relative deviations are as follows:

$$\text{IOF} : (0.230 - 0.213) * 100\%/0.213 = 8.0\%$$

$$\text{RAD} : (0.043 - 0.040) * 100\%/0.040 = 7.5\%$$

As a result the reflectance spectra discussed throughout the present paper can only be interpreted as relative spectra. Therefore, in most cases the spectra to be compared to each other have been scaled by a multiplicative factor to a common value at 440 nm.

[104] Because of reasons mentioned above the relative uncertainty of these spectra is not much smaller than 10% of the reflectance value. For example, if the scaled reflectance is 0.30 or 30% at 754 nm, the uncertainty amounts to 10% of that value, i.e., 0.03 or 3%.

Appendix D: RAT Simulator

[105] Preliminary tests on a number of samples (including the ones described here) have been performed on a specially designed premission RAT simulator, before the engineering model of the RAT (RAT-EM) was available. Part of the hysteresis data presented in the main section has also been acquired on abraded rock that has been generated by the RAT simulator. Therefore it seems appropriate to provide a brief description of that simulator. See Figure D1. The RAT simulator is mounted on one end of a balance allowing the force applied during grinding to be controlled by loading the setup with appropriate weights. The force of the grinding tool against the rock in the experiments performed here is less than 1 N in all cases and the rotation speed of the grinding tool

Table B1. Lighting and Viewing Geometry of RAT Images Acquired on A068 and B048[a]

	Position Vectors[b]		Angles,[c] deg			
Sol, Filter	$\hat{S}$	$\vec{L}$	i_{RAT}	e_{RAT}	g	Ψ
A068, L6	S_x = 0.13123743, S_y = −0.82839991, S_z = 0.54454598	L_x = 0.57779012, L_y = −0.072423818, L_z = 0.89154951	57.01	33.15	54.31	73.85
B048, L6	S_x = 0.42247333, S_y = −0.56474323, S_z = 0.70892974	L_x = 0.67110124, L_y = −0.059745238, L_z = 0.75123941	44.85	41.89	32.63	48.11

[a] $\hat{S}$, normalized Sun vector (expressed in RAT coordinates), S = 1; $\vec{L}$, position of Pancam left eye (expressed in RAT coordinates), $L = (L_x^2 + L_y^2 + L_z^2)^{1/2}$; incidence angle, $i_{RAT} = \cos^{-1}(S_z)$; emission angle, $e_{RAT} = \cos^{-1}(L_z/L)$; azimuthal angle (Figure B1), $\Psi = \cos^{-1}\{(L_xS_x + L_yS_y)/((L_x^2 + L_y^2)^{1/2}(S_x^2 + S_y^2)^{1/2})\}$; angles i_{RAT}, e_{RAT}, and Ψ, the RAT revolved housing cap plane; phase angle, $g = \cos^{-1}[\vec{L} \cdot \hat{S}/(LS)] = \cos^{-1}[\vec{L} \cdot \hat{S}/L]$.

[b] Inferred from MER SPICE kernels.

[c] Calculated from position vectors.

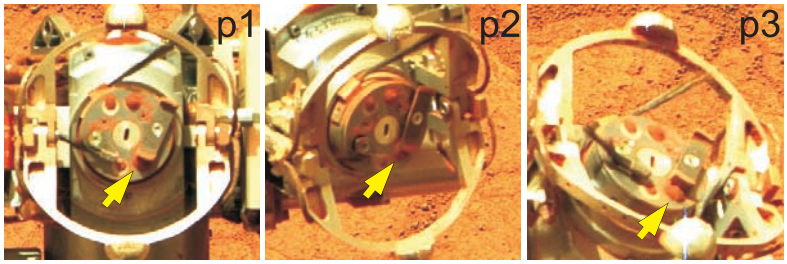

Figure C1. False color composite images (L2, L5, L7) of the RAT revolve housing, acquired at three different positions (p1, p2, p3) on B548. The arrows point to the sunlit part of RAT magnet 1_3 (compare spectra shown in Figure C2). The color images have been generated in a controlled way (with the RGB components stretched from 0 to 0.04 W m^{-2} sr^{-1} nm^{-1}).

(an abrasive diamond disk mounted on a Maxon electromotor) is typically 7000 rpm during operation. The rock being abraded is mounted on the pen mount of a plotter, programmed to emulate the planetary motion of the grinding wheel of the MER RAT. Thereby production of local heat on the rock surface and potential (chemical or magnetic) alteration of the rock material is minimized. A micrometer dial is used to limit the z range of the grinding tool, i.e., the maximum depth of grinding. The total mass of the rock abrasion material generated, density of the massive rock and area of the grinded surface allows some rough estimation of the grinding depth.

[106] The simulator has a diamond grinding disk (25.4 mm in diameter) working through a central hole in a plate that carries the RAT magnets (34 mm from the center of this disk). The four RAT magnets in the RAT simulator are identical to the RAT magnets on the rovers.

[107] After completion of a grinding session, the plate with the magnets is removed from the setup and imaged using a standard digital camera. The abraded material and (if possible) its magnetic extract (as accumulated on the magnets) are then subjected to further studies, such as transmission Mössbauer spectroscopy and investigation by a vibrating-sample magnetometer.

[108] Note the fundamental difference in terms of grinding: While the true RAT works its way into the rock removing grain by grain, the RAT simulator actually polishes the rock surface. After some "grinding time" the rock surface needs to be roughened again for more abrasion material to be produced. Therefore, in the case of the RAT simulator, the grinding time is not proportional to the grinding depth achieved. We may also expect some differences in grain size of the abraded material. However, the size distributions turn out to be rather similar for both grinding techniques and, in the case of basalts, they are dominated by 1 to 10 μm large particles. The most prominent difference remains the superior particle production rate and grinding efficiency of the RAT-EM as compared to the RAT simulator. Despite its simplicity and weakness the RAT simulations were reproducible and did produce a number of features that were later observed during grinding with the RAT-EM.

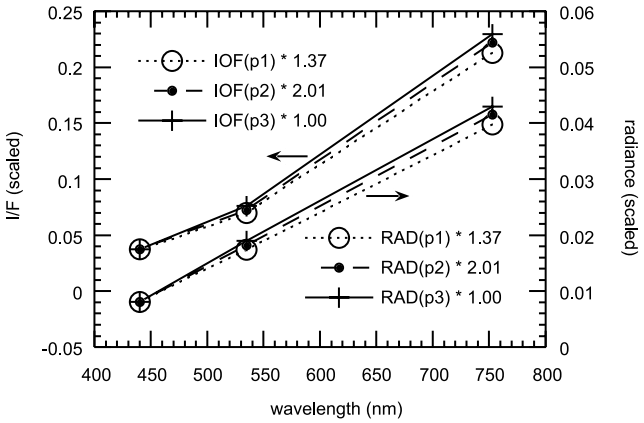

Figure C2. I/F (left ordinate) and radiance spectra (right ordinate) of the strong RAT magnet 1_3 on B548 for three different lighting-viewing geometries labeled p1, p2, and p3, respectively (compare Figure C1). All spectra are scaled to a common value at 440 nm.

Appendix E: Impact of Gravity on the RAT Magnet Experiment

[109] The RAT instrument had different orientations during grinding into Martian rocks. In particular for grindings early in the mission, the angle between the RAT centerline

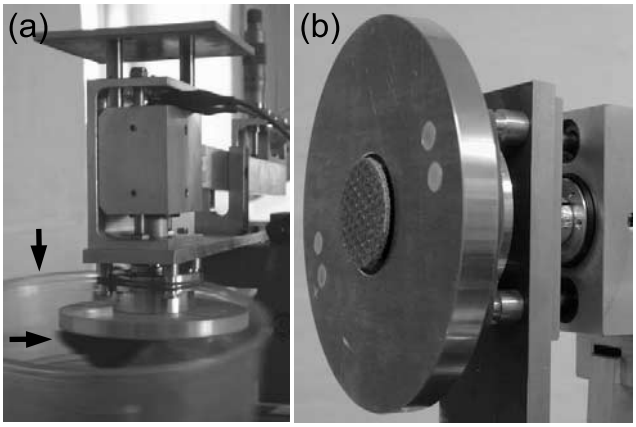

Figure D1. RAT simulator. (a) The grinding tool (foreground) that is mounted on one end of a balance. The micrometer dial (background) controls the maximum vertical motion of the grinder. The rock (horizontal arrow) is fixed on the pen mount of a plotter (not shown). A plastic container (vertical arrow) is used to collect the abrasion material (material not captured by the RAT magnets). (b) Close up of the diamond grinding disk (25.4 mm in diameter) that is mounted in the center of a plate carrying the RAT magnets.

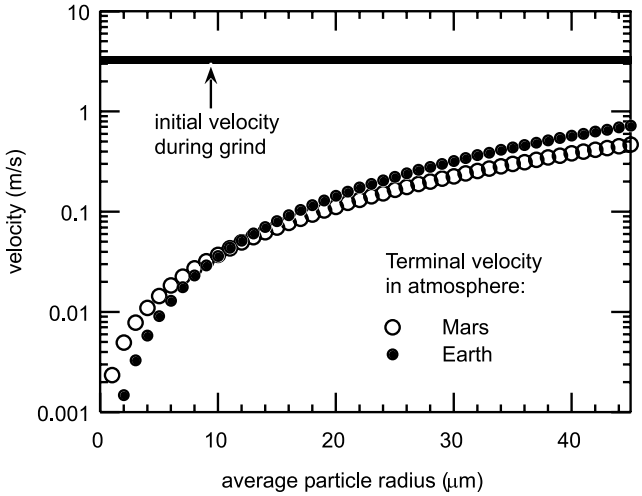

Figure E1. Relevant velocities during RAT grinding versus average particle radius.

vector (pointing in the grind direction) and the rover's z basis vector (pointing downward) were as follows: A034, 48°; A059, 66°; B030, 23°; B034, 46°; B044, 15°. However, most grind simulations in the laboratory have been performed with the RAT pointing downward (~0°). Naturally the question arises, how the difference in RAT orientation and in particular the difference in gravity may affect the conclusions that are based either on comparison between different grindings on Mars or on comparison between Earth and Mars. For simplicity, we will restrict the discussion to the strong RAT magnet (RAT magnet 1).

[110] As soon as a rock particle has been liberated during grinding, its trajectory may be affected by gravity. In the favorable case, this trajectory leads to the active surface of the RAT magnet, where the particle will either be trapped or rebound. In this appendix, we will (1) describe the relevant forces that act on the eroded rock particle, (2) discuss how gravity may influence the trajectory, and (3) discuss how it may influence the ability of the RAT magnet to absorb the particle's kinetic energy.

E1. Forces Acting on a Particle

[111] Let an eroded rock particle have mass m and average radius r. In some cases, it is useful to express the particle's mass as the product of volume and density: $m(r) = 4\pi r^3 \rho_{part}/3$ with $\rho_{part} \sim 3000$ kg m^{-3} for grains dominated by silicates. The term "average particle radius" denotes the radius of, e.g., the equal volume sphere of a given irregular particle, and should not be confused with the average of an entire particle size distribution.

[112] Such a particle is subjected to three dominant forces, i.e., the gravitational force (F_G), the magnetic force (F_M) and the atmospheric drag (F_D) [*Kinch*, 2005]:

$$\vec{F}_G(r) = m(r) \cdot \vec{g}, \tag{E1}$$

$$\vec{F}_M(r) = m(r)\sigma(B) \cdot \vec{\nabla} B, \tag{E2}$$

$$\vec{F}_D(r) = \frac{6\pi\mu r \cdot \vec{v}}{S(r)}, \quad S(r) = 1 + \frac{\lambda}{r}\left[1.257 + 0.4\exp\left(-1.1\frac{r}{\lambda}\right)\right], \tag{E3}$$

Here μ is the dynamical viscosity of the atmosphere (Mars, $\mu = 12.6 \times 10^{-6}$ kg m^{-1} s^{-1}; Earth, $\mu = 18.3 \times 10^{-6}$ kg m^{-1} s^{-1}), v is the particle velocity with respect to atmosphere and λ is the mean free path of gas molecules in the atmosphere (Mars, $\lambda = 6.87$ μm; Earth, $\lambda = 6.63 \times 10^{-2}$ μm). Typical atmospheric conditions are assumed (Mars, CO_2, 750 Pa, 250 K; Earth, air, 0.1013 MPa, 293 K).

[113] Equation (E1) is always valid. Equation (E2) assumes that the magnetization of the particle is perfectly aligned with the local magnetic field. The gravitational force is independent of the particle's position, while the magnetic force becomes significant only in the vicinity of the RAT magnet (say at a distance smaller than a few millimeters from the center of its active area).

[114] Equation (E3) is Stokes' law as modified by *Davies* [1945], who introduced a dimensionless correction factor $S(r) \geq 1$, the so-called slip factor. Stokes' law has been derived for slowly moving, spherical particles in a continuous fluid medium. Davies' empirical correction is needed, whenever the molecular nature of the fluid becomes apparent, as, e.g., in the case of very small particles moving in low-pressure gases. Although Stokes and Davies' formulas have been developed on the example of spherical particles, they should still be useful approximations for irregular particles as well, with an expected accuracy of better than a factor of 2. One can check that the slip factor is quite important for micron-sized particles on Mars (e.g., $S > 1.1$ if $r < 80$ μm, and $S > 10$, if $r < 1$ μm), while it can be neglected for particles of similar size on Earth. Note that (E3) requires laminar gas flow (or, equivalently, small Reynold's numbers) near the particle surface. Let us assume that a newly generated rock particle has a typical (initial) velocity (denoted v_0) that is similar to the one of the grinding bit: $v_0 \sim D\pi\nu \sim 3.3$ m/s, where D is the distance between both grinding bits ($D \sim 21$ mm) and ν is the rotational frequency of the grinding paddle that carries bits ($\nu = 50$ Hz). In that case the Reynolds numbers are in the range $0.004 \sim 0.2$ and $0.2 \sim 12$ for Mars and Earth, respectively, depending on assumed particle size. We conclude that these flows are truly laminar in either environmental condition.

E2. Influence of Gravity on the Trajectory of a Particle

[115] Let us first consider a freely falling particle in the Martian or terrestrial atmosphere. Initially, this particle will be accelerated, and after a characteristic time it will reach a constant, terminal velocity (denoted v_T), where atmospheric drag equals gravitational force:

$$v_T = \frac{2 \cdot S(r) \cdot r^2 \cdot \rho_{part.} \cdot g}{9 \cdot \mu} \tag{E4}$$

The terminal velocity is shown as a function of particle radius in Figure E1. Most particle radii seem to be in the range 1–10 μm, although particle radii up to 50 μm have been observed. The initial velocity of an eroded rock

particle is assumed to be similar to the rotational velocity of the grind paddle ($\sim$3.3 m s^{-1}). Terminal velocities of freely falling particles are thus at least by an order of magnitude smaller than the initial particle velocity.

[116] Note in addition that this terminal velocity is only reached after some characteristic time, which may be longer than the one needed to escape or to be captured by the RAT magnet.

[117] We conclude that gravity, either on Earth or on Mars, cannot significantly bend the particles' trajectory and that the trajectory is independent of the particular RAT orientation during grinding.

E3. Influence of Gravity on the Capture of a Particle

[118] Now we will investigate, if the actual capture of an incoming particle (i.e., the absorption of the particle's kinetic energy) can be influenced by gravity. Obviously, the capture is enabled by the magnetic force. From (E1) and (E2) it can be seen that the accelerations due to gravitational and magnetic force are given by g and $\sigma(B) \cdot |\vec{\nabla}B|$, respectively. Thus, instead of comparing these two forces, we can as well compare the two associated accelerations. The gravitational accelerations on Earth and on Mars may be taken as 9.81 and 3.69 m s^{-2}, respectively.

[119] Rock grinding experiments performed in the laboratory as well as on the surface of Mars generated 1 to 2 mm thick accumulations of magnetic particles. The strong RAT magnet is designed such that particles located within the volume of these accumulations experience a magnetic field gradient of at least 50 T m^{-1} (Figure 1). Thus, for a particle magnetization of 0.5 A m^2 kg^{-1} the acceleration due to magnetic forces is at least 25 m s^{-2}. Particles that are positioned closer to the active surface of the magnet encounter a larger magnetic field gradient (up to 350 T m^{-1}) and thus experience a correspondingly larger acceleration due to magnetic forces. It can be seen that even the lower bound to this acceleration is somewhat larger than the accelerations due to gravity on Earth or Mars (Gusev plains, Meridiani outcrops).

[120] Note that we do not say that particles with a favorable trajectory and a magnetization of 0.5 A m^2 kg^{-1} are necessarily captured by the magnet, but just assess the potential influence of gravity. Obviously, the grinding process generates particles with a broad range of magnetizations. As a consequence, many of these particles do have a magnetization below 0.5 A m^2 kg^{-1} nearby the magnet. However, it has been established by analysis of simulation experiments (compare section 4.4) that such particles could not be captured anyway due to the significant velocity of the incoming particle.

[121] We conclude that gravity should not have a strong effect on the amount of material clinging to the strong RAT magnet, although it may pull away some of the outermost, weakly bound parts of the material on the RAT magnet, in particular in combination with robotic arm motion. This argument should apply both to experiments on Mars and to simulations on Earth. However, the margin is much larger on Mars as compared to Earth. As a result, RAT orientation during grinding on Mars is insignificant, while RAT simulations on Earth should always be performed with the same RAT orientation such that the small (though detectable) influence of gravity is always the same. The gravity vector points downward, while the magnetic field gradient is largely oriented along the RAT centerline. Therefore all simulations on Earth should be (and have been) performed with the RAT instrument pointing vertically downward. In that case the projection of the magnetic force onto the direction of the gravitational force is largest, whereby the potential impact of gravity is minimized.

Notation

This list is not complete but should support the understanding of section 2. Selected symbols are grouped according to their physical meaning rather than being listed alphabetically. Abbreviations are RH, rh, RAT revolve housing; RHCP, revolve housing cap plane of the RAT.

I	radiance [W m^{-2} nm^{-1} sr^{-1}].
A_L, B_L	model parameters (Lambert's law) [W m^{-2} nm^{-1} sr^{-1}].
i_{RAT}	solar incidence angle on the RHCP (compare Figure 4).
e_{RAT}	angle of emergence for that plane, i.e., angle between normal to that plane and direction to Pancam left eye.
i	solar incidence angle on a local facet of the RAT magnet particle accumulation (compare Figure 4).
e	angle of emergence for that particular local facet (actually not used).
θ	slope of that particular local facet (compare Figure 4).
Ψ	angle between direction of incident solar light as projected onto the RHCP and direction to Pancam left eye as projected onto the RHCP (compare Figure B1).
Ψ'	same as Ψ, but referring to the corresponding angle in image space.
ϕ	angle between direction of incident solar light as projected onto the RHCP and profile across the RAT magnet particle accumulation as projected onto the RHCP.
ϕ'	same as ϕ, but referring to the corresponding angle in image space.
a_{rh}	major demiaxis [px] of RH ellipse, as seen in the image.
b_{rh}	minor demiaxis [px] of RH ellipse (as seen in the image), coinciding with the direction to Pancam left eye as projected onto the RHCP.
d_{rh}	diameter [mm] of RH (d_{rh} = 33.4 mm).
α'	angle between vertical direction in the image and major demiaxis of the RH ellipse.
β'	angle between vertical direction in the image and straight-line pixel profile selected for radiometric analysis, thus $\beta' = \alpha' + (90° - \Psi') + \phi'$.
a	major demiaxis [px] of RAT magnet particle ellipse, as seen in the image.
b	minor demiaxis [px] of RAT magnet particle ellipse, as seen in the image, $b/a = b_{rh}/a_{rh}$.
h	height [mm] of RAT magnet particle accumulation.

[122] **Acknowledgments.** The authors are indebted to the Pancam team and the rover drivers for their efforts to perform RAT magnet imaging

at a favorable lighting-viewing geometry. This turned out to be very important. A grant for W. G. from the Danish Natural Science Research Council (2002–2003) as well as support from the Departments of the Niels Bohr Institute (January–April 2004) made some of the experimental part of this work possible. Also support from the University of Copenhagen for C. S. B. is gratefully acknowledged. The final manuscript was substantially improved due to the excellent review work by Gunther Kletetschka and another (anonymous) scientist.

References

Bell, J. F., III, T. B. McCord, and P. D. Owensby (1990), Observational evidence of crystalline iron oxides on Mars, *J. Geophys. Res.*, *95*, 14,447–14,461.

Bell, J. F., III, et al. (2003), Mars Exploration Rover Athena Panoramic Camera (Pancam) investigation, *J. Geophys. Res.*, *108*(E12), 8063, doi:10.1029/2003JE002070.

Bell, J. F., III, J. Joseph, J. N. Sohl-Dickstein, H. M. Arneson, M. J. Johnson, M. T. Lemmon, and D. Savransky (2006), In-flight calibration and performance of the Mars Exploration Rover Panoramic Camera (Pancam) instruments, *J. Geophys. Res.*, *111*, E02S03, doi:10.1029/2005JE002444.

Connerney, J. E. P., M. H. Acuña, P. Wasilewski, N. F. Ness, H. Rème, C. Mazelle, D. Vignes, R. P. Lin, D. Mitchell, and P. Cloutier (1999), Magnetic lineations in the ancient crust of Mars, *Science*, *284*, 794–798.

Craddock, R. A., T. A. Maxwell, and A. D. Howard (1997), Crater morphometry and modification in the Sinus Sabaeus and Margaritifer Sinus regions of Mars, *J. Geophys. Res.*, *102*, 13,321–13,340.

Davies, C. N. (1945), Definitive equations for the fluid resistance of spheres, *Proc. Phys. Soc.*, *57*(4), 259–270.

Davis, P. A., and L. A. Soderblom (1984), Modeling crater topography and albedo from monoscopic Viking orbiter images, *J. Geophys. Res.*, *89*, 9449–9457.

Dunlop, D. J., and Ö. Özdemir (1997), *Rock Magnetism, Fundamentals and Frontiers*, Cambridge Univ. Press, New York.

Farrand, W. H., et al. (2007), Visible and near-infrared multispectral analysis of rocks at Meridiani Planum, Mars, by the Mars Exploration Rover Opportunity, *J. Geophys. Res.*, *112*, E06S02, doi:10.1029/2006JE002773.

Gellert, R., et al. (2004), Chemistry of rocks and soils in Gusev Crater from the Alpha Particle X-ray Spectrometer, *Science*, *305*, 829–832.

Goetz, W., et al. (2005), Indication of drier periods on Mars from the chemistry and mineralogy of atmospheric dust, *Nature*, *436*, 62–65.

Gorevan, S. P., et al. (2003), Rock Abrasion Tool: Mars Exploration Rover mission, *J. Geophys. Res.*, *108*(E12), 8068, doi:10.1029/2003JE002061.

Gunnlaugsson, H. P., S. F. Hviid, J. M. Knudsen, and M. B. Madsen (1998), Instruments for the magnetic properties experiments on Mars Pathfinder, *Planet. Space Sci.*, *46*, 449–459.

Hapke, B. (1993), *The Theory of Reflectance and Emittance Spectroscopy*, Cambridge Univ. Press, New York.

Horn, B. K. P., and M. J. Brooks (Eds.) (1989), *Shape From Shading*, MIT Press, Cambridge, Mass.

Kinch, K. M. (2005), Numerical modeling of magnetic capture of Martian atmospheric dust, Ph.D. thesis, Univ. of Aarhus, Aarhus, Denmark.

Kinch, K. M., J. Sohl-Dickstein, J. F. Bell III, J. R. Johnson, W. Goetz, and G. A. Landis (2007), Dust deposition on the Mars Exploration Rover Panoramic Camera (Pancam) calibration targets, *J. Geophys. Res.*, *112*, E06S03, doi:10.1029/2006JE002807.

Kletetschka, G., and P. J. Wasilewski (2002), Grain size limit for SD hematite, *Phys. Earth Planet. Inter.*, *129*, 173–179.

Kletetschka, G., P. J. Wasilewski, and P. T. Taylor (2000a), Hematite vs. magnetite as the signature for planetary magnetic anomalies?, *Phys. Earth Planet. Inter.*, *119*, 259–267.

Kletetschka, G., P. J. Wasilewski, and P. T. Taylor (2000b), Mineralogy of the sources for magnetic anomalies on Mars, *Meteorit. Planet. Sci.*, *35*, 895–899.

Klingelhöfer, G., et al. (2004), Jarosite and hematite at Meridiani Planum from Opportunity's Mössbauer spectrometer, *Science*, *306*, 1740–1745.

Larsen, L. M., and A. K. Pedersen (2000), Processes in high-Mg, high-T magmas: Evidence from olivine, chromite and glass in Palaeogene picrites from West Greenland, *J. Petrol.*, *41*(7), 1071–1098.

Leer, K., B. Basso, C. Binau, W. Goetz, S. Gorevan, S. F. Hviid, A. Kusack, M. B. Madsen, S. W. Squyres, and J. Wilson (2006), Simulating collection of dust on the RAT magnets onboard the Mars Exploration Rovers, *Lunar Planet. Sci. Conf.*, *XXXVII*, Abstract 1784.

Lemmon, M., et al. (2004), Atmospheric imaging results from the Mars Exploration Rovers: Spirit and Opportunity, *Science*, *306*, 1753–1756.

Madsen, M. B., et al. (2003), Magnetic Properties Experiments on the Mars Exploration Rover mission, *J. Geophys. Res.*, *108*(E12), 8069, doi:10.1029/2002JE002029.

Maki, J. N., et al. (2003), Mars Exploration Rover Engineering Cameras, *J. Geophys. Res.*, *108*(E12), 8071, doi:10.1029/2003JE002077.

McSween, H. Y. (1985), SNC meteorites: Clues to Martian petrologic evolution?, *Rev. Geophys.*, *23*, 391–416.

Morris, R. V., et al. (2004), Mineralogy at Gusev Crater from the Mössbauer spectrometer on the Spirit Rover, *Science*, *305*, 833–836.

Morris, R. V., et al. (2006a), Mössbauer mineralogy of rock, soil, and dust at Gusev crater, Mars: Spirit's journey through weakly altered olivine basalt on the plains and pervasively altered basalt in the Columbia Hills, *J. Geophys. Res.*, *111*, E02S13, doi:10.1029/2005JE002584.

Morris, R. V., et al. (2006b), Mössbauer mineralogy of rock, soil, and dust at Meridiani Planum, Mars: Opportunity's journey across sulfate-rich outcrop, basaltic sand and dust, and hematite lag deposits, *J. Geophys. Res.*, *111*, E12S15, doi:10.1029/2006JE002791.

Mustard, J. F., and J. F. Bell (1994), New composite reflectance spectra of Mars from 0.4 to 3.14 μm, *Geophys. Res. Lett.*, *21*, 353–356.

Rieder, R., et al. (2004), Chemistry of rocks and soils at Meridiani Planum from the Alpha Particle X-ray Spectrometer, *Science*, *306*, 1746–1749.

Roberts, A. P., Y. L. Cui, and K. L. Verosub (1995), Wasp-waisted hysteresis loops–mineral magnetic characteristics and discrimination of components in mixed magnetic systems, *J. Geophys. Res.*, *100*, 17,909–17,924.

Rochette, P., J. P. Lorand, G. Fillion, and V. Sautter (2001), Pyrrhotite and the remanent magnetization of SNC meteorites: A changing perspective on Martian magnetism, *Earth Planet. Sci. Lett.*, *190*, 1–12, doi:10.1016/S0012-821X(01)00373-9.

Singer, R. B., T. B. McCord, R. N. Clark, J. B. Adams, and R. L. Hugueni (1979), Mars surface composition from reflectance spectroscopy: A summary, *J. Geophys. Res.*, *84*, 8415–8426.

Squyres, S. W., et al. (2003), Athena Mars rover science investigation, *J. Geophys. Res.*, *108*(E12), 8062, doi:10.1029/2003JE002121.

Squyres, S. W., et al. (2004), The Opportunity Rover's Athena science investigation at Meridiani Planum, Mars, *Science*, *306*, 1698–1703.

Tauxe, L., T. A. T. Mullender, and T. Pick (1996), Potbellies, wasp-waists, and superparamagnetism in magnetic hysteresis, *J. Geophys. Res.*, *101*, 571–583.

Yen, A. S., et al. (2005), An integrated view of the chemistry and mineralogy of Martian soils, *Nature*, *436*, 49–54.

P. Bartlett, B. Basso, P. C. Chu, S. Gorevan, A. Kusack, E. Mumm, T. Myrick, and J. Wilson, Honeybee Robotics, 460 W. 34th St., New York, NY 10001, USA.

J. Bell, K. M. Kinch, and S. W. Squyres, Department of Astronomy, Cornell University, Ithaca, NY 14853-6801, USA.

P. Bertelsen, C. S. Binau, K. Leer, M. B. Madsen, and M. Olsen, Niels Bohr Institute, University of Copenhagen, Copenhagen, DK-2100, Denmark.

W. Goetz and S. F. Hviid, Max-Planck-Institut für Sonnensystemforschung, Katlenburg-Lindau, D-37191, Germany. (goetz@mps.mpg.de)

H. P. Gunnlaugsson, Institute of Physics and Astronomy, University of Aarhus, Aarhus, DK-8000, Denmark.

M. F. Hansen, Department of Micro- and Nanotechnology, Danish Technical University, Kongens Lyngby, DK-2800 Kongens Lyngby, Denmark.

G. Klingelhöfer, Institute for Inorganic and Analytical Chemistry, Johannes Gutenberg-Universität, Staudingerweg 9, Mainz, D-55128, Germany.

D. W. Ming and R. V. Morris, NASA Johnson Space Center, Houston, TX 77058, USA.

A. Yen, Jet Propulsion Laboratory, California Institute of Technology, Mail Code 183-501,4800 Oak Grove Drive, Pasadena, CA 91109, USA.